Bachelor's Thesis

Molekulardynamik Simulationen von Blauen Phasen in Gleichgewicht und Nicht-Gleichgewicht

Molecular dynamics simulations of blue phases in equilibrium and nonequilibrium

prepared by

Vitali Telezki

from Shambyl (Kazakhstan)

at the Max Planck Institute for Dynamics and Self-Organization

NESM

Zusammenfassung

In dieser Arbeit werden höchst nicht-triviale Phasen von Flüssigkristallen, sog. *blue phases* mithilfe von Molekulardynamik Simulationen untersucht. Es wird dabei ein großer Phasenraum in Abhängigkeit von Druck, Temperatur und Chiralität analysiert. Das Hauptaugenmerk wird hierbei auf die Disklinationslinien gelegt, mit denen man kristallographische Symmetrien identifizieren kann. Außerdem wird das System im Nicht-Gleichgewichtszustand im Fluss untersucht.

Stichwörter: Physik, Flüssigkristalle, Molekulardynamik Simulationen, Blaue Phase, Gleichgewicht, Nicht-Gleichgewicht.

Abstract

The key focus of this work is the analysis of highly non-trivial blue phases of chiral liquid crystals via molecular dynamics simulations. As a result the dependencies of structure and thermodynamic phases on pressure, temperature and the chirality are presented. Furthermore, crystallographic symmetries are identified with the visualization of disclination lines. In addition, we drive the system out of equilibrium with an added constant hydrodynamic flow.

Keywords: physics, liquid crystals, molecular dynamics simulations, blue phases, disclination lines, equilibrium, nonequilibrium.

Contents

Contents

1 Introduction

Liquid crystals can be found both in the natural world and in technological applications. A ubiquitous presence is the contemporary liquid crystal display technology used in modern applications. Also biological systems offer examples of liquid crystals, for example many proteins, cell membranes or spider silk are made out of molecules exhibiting liquid crystalline phases.

In this work we will study the thermodynamic phases and dynamics of molecules which exhibit chiral behaviour. An outstanding and interesting phase occurs between the cholesteric and the isotropic phase of highly chiral thermotropic liquid crystals: the blue phase. Its orientational order can be characterized by crystallographic space group symmetries, with a typical lattice size in the regime of visible light. The selective Bragg scattering makes this phase especially interesting for optical purposes.

This thesis will briefly introduce liquid crystals and its different phases and will then concentrate on the description, both phenomenologically and mathematically, of blue phases in chiral liquid crystals.

1.1 Liquid Crystals

From our every day experience we have learned that matter undergoes phase changes. The most common states are the solid, liquid and the gas state. One might think that these are also the only ones. But this is not quite correct. Certain materials do not show a single transformation from solid to liquid, but undergo a cascade of transitions to new, intermediate phases [1]. Thereby they exhibit mechanical and symmetry properties that are intermediate between those of a liquid and a crystal. For this reason they have been called *liquid crystals*, or *mesomorphic phases*.

But what are the properties of a crystal and of a liquid? A crystal can be described by a three-dimensional periodic array of identical building blocks, apart from any imperfections and impurities that may occur [2]. This results in sharp Bragg peaks

in X-ray scattering. In contrast to that, one cannot find those Bragg peaks in a conventional liquid. This is related to the fact that positional order in a liquid is lost over a typical length scale ξ. Moreover a liquid is able to flow easily, in contrast to the solid nature of a crystal.

A liquid crystal is made of molecules with anisotropic shape and a rigid core that is typically composed of aromatic rings. The molecules of a liquid crystal exhibit different degrees of positional or orientational order in at least one dimension. The then remaining degrees of freedom characterize the different phases of liquid crystals.

Different types of liquid crystals can be observed in nature, depending on the structure of the molecules. Without delving too deeply into the chemical properties and details, we can distinguish between liquid crystals that have a phase transition due to temperature change, *thermotropic*, and those that have a phase transition due to changing the concentration of the molecules in a suitable solvent, *lyotropic*. Furthermore, the shape of the liquid crystals dictates the different states. Rod-like molecules, such as PPA or MBBA (see Fig. 1.1), exhibit the so-called *nematic* state, whereas cholesterol esters exhibit the *cholesteric* state. In contrast to that disk-like molecules arrange themselves in columnar phases. The focus of this work shall lie in the thermotropic rod-like liquid crystals.
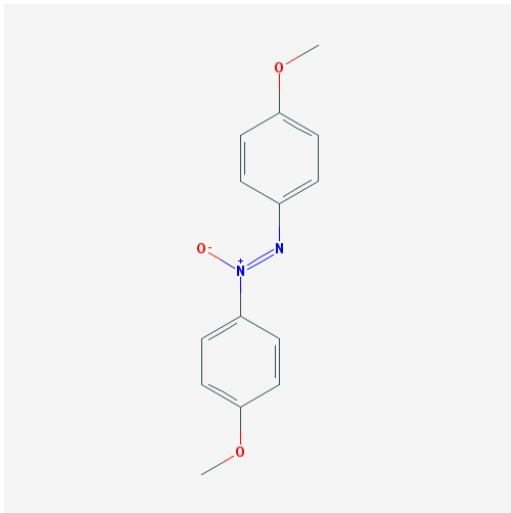
(a) Formula of p-azoxyanisole (PAA), which is approximately a rod of the length $\sim 20\,\text{Å}$ and a width of $\sim 5\,\text{Å}$.
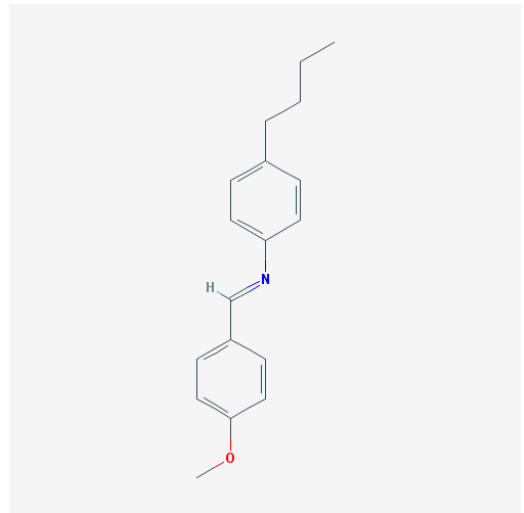
(b) Formula of N-(p-methoxybenzylidene)-p-butylaniline, a typical nematogen.

Figure 1.1: Structure formulas of typical liquid crystal molecules PPA [3] and MBBA [4].

1.1.1 Nematics

In a nematic phase, the centers of gravity of the molecules have no long-range order, but the orientations of the molecules have one preferred direction, in contrast to a conventional liquid. All the molecules tend to align parallel to an arbitrary chosen axis in space, labeled by a unit vector, the so called director $\hat{\boldsymbol{n}}$, as shown in Fig. 1.2. Furthermore the molecules are head-tail symmetric, so the states of the director $\hat{\boldsymbol{n}}$ and $-\hat{\boldsymbol{n}}$ are not distinguishable, or if they are, there are as many particles pointing up as there are particles pointing down.

It can be observed that nematic phases only occur for particles, that are achiral or *racemic* (with equal numbers of left- and right-handed molecules) [1].
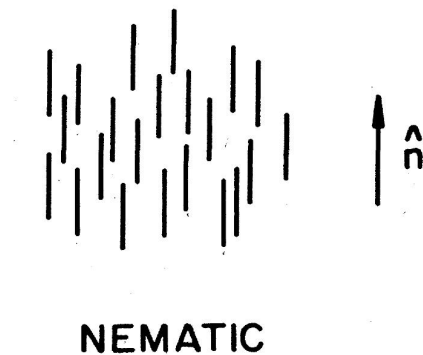

Figure 1.2: Schematic representation of an uniform director field in the nematic phase [5].

1.1.2 Cholesterics

Cholesteric[1] liquid crystals are also known as chiral nematic liquid crystals. A chiral object is defined as an object with a geometrical structure different from its mirror image, as for example human hands are. Cholesterics organize themselves in nematic layers, where the director axis varies with the layers. This variation tends to be periodic, and therefore a helical structure forms (see Fig. 1.3). Due to this helical structure this phase will further be referred to as the helical phase. Since the director $\hat{\boldsymbol{n}}$ is not constant in space but periodic, it can be described by a rotation

---

[1]The name *cholesteric* refers to cholesterol esters, which are chiral, where this kind of helical distortion was first observed.
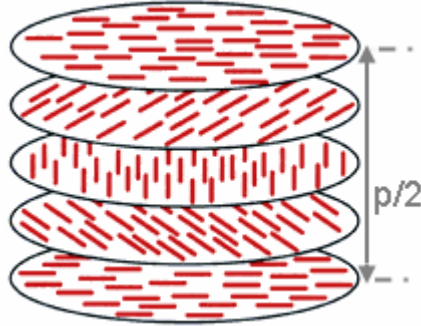
Figure 1.3: Schematic representation of a cholesteric phase of rod-like molecules. The director rotates about 180° over the corresponding distance of half of a pitch $p/2$ [6].

around its helical axis z:

$$n_x = \cos(q_0 z + \phi) \tag{1.1a}$$

$$n_y = \sin(q_0 z + \phi) \tag{1.1b}$$

$$n_z = 0. \tag{1.1c}$$

Both the helical axis z and ϕ are arbitrary. The spatial period L is equal to one-half of the pitch:

$$L = \frac{\pi}{|q_0|}, \tag{1.2}$$

where $q_0 = q_0(T)$ is a function of temperature and is a measure of the chirality. Typical values for L are about $3000\,\text{Å}$, which lies in the optical wavelength, due to the periodicity it results in Bragg diffractions of light beams [1].

1.1.3 Blue Phase

Chiral liquid crystals also form blue phases, at temperatures immediately below the transition from the isotropic phase, but not all chiral liquid crystals have blue phases [5]. They received their name from their blue appearance in early investigations, but they are not always blue [7]. Blue phases are divided into three different groups, which are called BP I, BP II and BP III, which are all thermodynamically distinct phases and not metastable forms of the helical phase [5]. As shown in Fig. 1.4, the transition region is a narrow temperature region of approximately $1\,\text{K}$.
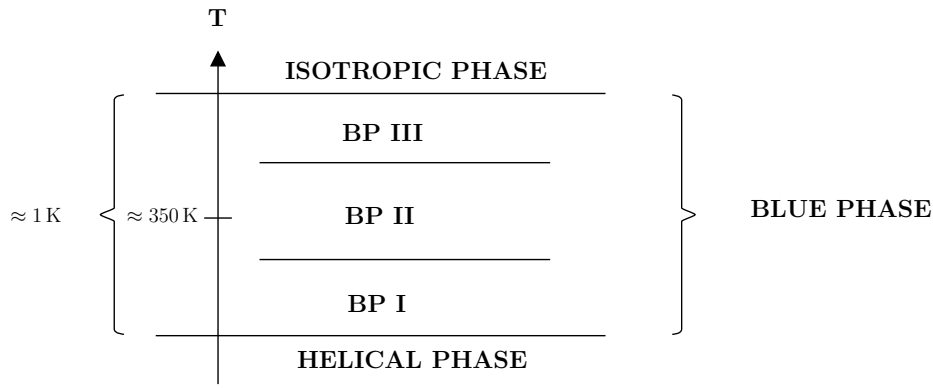
Figure 1.4: Schematic phase diagram showing the occurrence of blue phases in relation to the helical and the isotropic phases to emphasize the narrow temperature region of $\sim 1\,\mathrm{K}$ [5].

It was shown that both a latent heat (see Fig. 1.5) and a density change at the blue-helical transition can be observed [8]. Especially the heat-capacity measurements prove that the three different blue phases are indeed three distinct phases with clearly visible phase transitions in the expected narrow temperature region. Furthermore, it was shown that all the transitions are of first order [9].
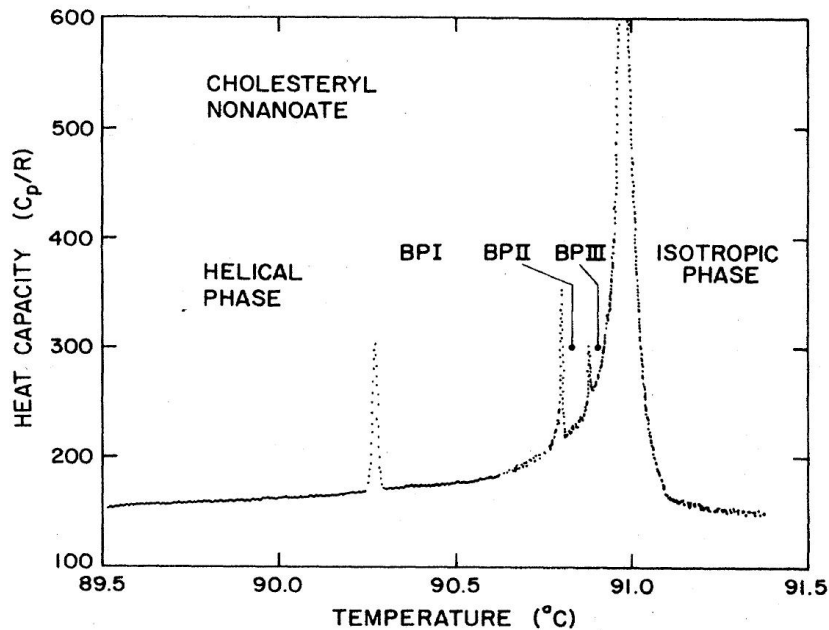

Figure 1.5: High-resolution heat-capacity measurements for the blue-phase region of cholesteryl nonanoate [9]. General overview for the entire temperature range, covering all phase transitions involving blue phases, with clearly visible peaks when the phase transitions happen.

Additionally blue phases exhibit a non-zero elastic shear modulus, although they flow like a liquid, with a bulk viscosity roughly up to 10^6 times larger than for a conventional liquid [10]. This shear modulus is about one million times smaller than that of a conventional solid [11, 12].

But why do blue phases occur? The fundamental cause for the helical phase is that the molecules themselves are chiral. Twist arises because the interaction energy of two adjacent molecules is minimized, when they are tilted of a slight angle to each other. This condition is met only for one axis in the helical phase (Fig. 1.3). However, the energy can be further minimized, when the twist also occurs in all directions perpendicular to the local director. Such a configuration is called *double twist* and is shown in Fig. 1.6. However, fitting these double twist cylinders into a three-dimensional structure while conserving the director and securing a high filling fraction is topologically impossible [7].
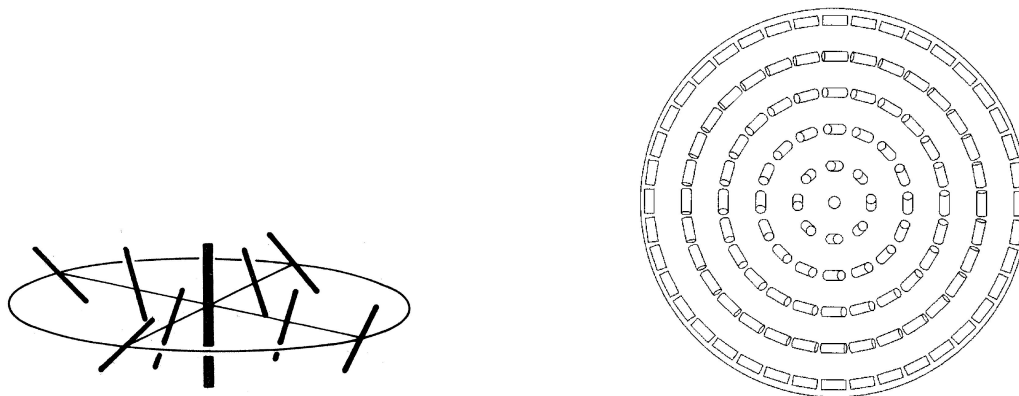
(a) Schematic representation of a double twist from D. Wright and N. D. Mermin [5]. The dark lines show the orientation of the director field. The configuration is cylindrically symmetric around the center of the figure.

(b) Cross-sectional view of a double twist from P. P. Crooker [7]. The director is parallel to the tube axis at the center and is twisting, as it approaches the edge.

Figure 1.6: Schematic view for double twist tubes in comparison.

Because a single double-twist cylinder is energetically unfavorable, the blue phases consist of many of these cylinders, arranged in a periodic lattice that corresponds with already known cubic symmetries, as shown in Fig. 1.7. To be more specific, BP I has body-centered cubic (bcc) orientational order and BP II a simple cubic (sc) order [7]. In contrast to the cubic structures of BP I and BP II, the structure of BP III may be characterized as a quasi-crystal [13], a spaghetti-like tangle of

double-twist cylinders [14] or an amorphous state formed by BP II domains [15]. Due to the different structures, polarized light gets deflected differently.
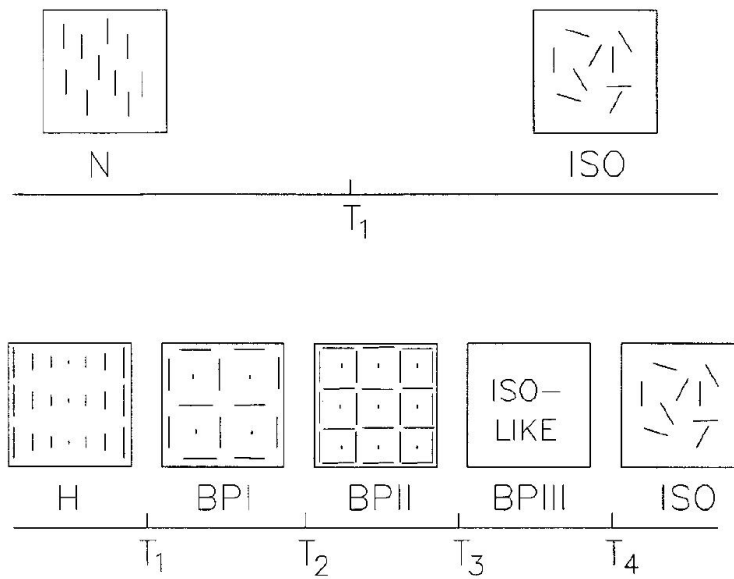
Figure 1.7: Schematic representation of the liquid crystal phases depending on the temperature. At the top non-chiral molecules are shown, which only have the nematic (N) and the isotropic (ISO) phase for higher temperatures. At the bottom the representation of chiral molecules shows the helical (H) and isotropic phase (ISO) and, depending on the chirality, up to three different blue phases (BP I, BP II and BP III). Whereas the BP I has a bcc and the BP II a sc structure [7]. The structure of the BP III is represented by a spaghetti-like tangle (iso-like) of double-twist cylinders.

2 Model System

2.1 Molecular Dynamics Simulations

In this chapter we shall briefly introduce the basic concepts of molecular dynamics (MD) simulations and its implementation.

MD simulations are often used for computing equilibrium and transport properties of an N particle system that follows the laws of classical physics [16]. The basic algorithm is usually as follows: At the time $t = 0$ N particles are initialized. This means, the initial positions and velocities are assigned. A common way is to pick these values randomly from a given distribution that fits the experimental circumstances. In the next step all the forces on all particles are being computed. The core of an MD simulation consists of the integration of Newton's equations of motion for each particle at each time step. The calculation of the force acting on every particle is also the most time-consuming part of almost all MD simulations [16]. In order to compute the force acting between the particles i and j, first their distance has to be calculated. Excluding long-range potentials, such as gravitational or Coulombic interactions, if the distance is smaller than a given cutoff radius r_c, the particles are close enough to each other to interact. The force acting between the particles comes directly from the given conservative potential $V(r)$,

$$\boldsymbol{F}(r) = -\nabla V(r).$$

Now that all forces between the particles are calculated, they can be used to integrate Newton's equations of motion to get the new particle positions and velocities after a small time step δt. The most common and effective algorithm is the velocity-Verlet algorithm for integration [16]. The updated positions and velocities can now be used to calculate the new forces between the particles. This step is being repeated until the desired simulation time is reached.

After the core part is completed, various quantities like temperature or pressure,

can be computed. In order to perform MD simulations in other than the microcanonical ensemble, a wide range of techniques has to be applied [16], like the use of a thermostat to fix the temperature of the system or the use of a barostat to fix the pressure of the system, just to name a few.

2.2 Potential Model

The potential used is the well studied Hess-Su potential [17] with the addition of chirality according to Memmer et al. [18, 19]. The liquid crystal is confined in one dimension between a pair of planar smooth walls where hybrid anchoring is employed.

The model consists of N liquid crystal molecules within a simulation box of linear sizes l_x, l_y, l_z. The total potential may be decomposed into contributions from the fluid-fluid (ff) and fluid-substrate (fs) interactions according to Melle et al.[20]:

$$\Phi\left(\boldsymbol{R},\hat{\boldsymbol{U}}\right) = \Phi_{ff}\left(\boldsymbol{R},\hat{\boldsymbol{U}}\right) + \Phi_{fs}\left(Z,\hat{\boldsymbol{U}}\right), \qquad (2.1)$$

with the shorthand notation, $Z \equiv \{z_1, z_2, \ldots, z_N\}$, for the z-coordinates of the center-of-mass positions, $\boldsymbol{R} \equiv \{\boldsymbol{r_1}, \boldsymbol{r_2}, \ldots, \boldsymbol{r_N}\}$, of the N mesogens and for their orientations represented by the set of unit vectors, $\hat{\boldsymbol{U}} \equiv \{\hat{\boldsymbol{u}}_1, \hat{\boldsymbol{u}}_2, \ldots, \hat{\boldsymbol{u}}_N\}$, where a caret will from now on be used to indicate a unit vector. The assumption of pairwise additivity of the interactions of the particles i and j with the center-of-mass distance $\boldsymbol{r}_{ij} \equiv \boldsymbol{r}_i - \boldsymbol{r}_j$ yields:

$$\Phi_{ff}\left(\boldsymbol{R},\hat{\boldsymbol{U}}\right) = \frac{1}{2}\sum_{i=1}^{N}\sum_{j\neq i}^{N}\varphi_{ff}\left(\boldsymbol{r}_{ij},\hat{\boldsymbol{u}}_i,\hat{\boldsymbol{u}}_j\right), \qquad (2.2)$$

with the chiral version of the Hess-Su potential:

$$\varphi_{ff}\left(\boldsymbol{r}_{ij},\hat{\boldsymbol{u}}_i,\hat{\boldsymbol{u}}_j\right) = 4\epsilon_{ff}\left\{\left(\frac{\sigma}{r_{ij}}\right)^{12} - \left(\frac{\sigma}{r_{ij}}\right)^{6}\left[1 + \Psi\left(\boldsymbol{r}_{ij},\hat{\boldsymbol{u}}_i,\hat{\boldsymbol{u}}_j\right)\right]\right\}, \qquad (2.3)$$

where σ is the particle diameter of a spherical Lennard-Jones reference particle and ϵ_{ff} the potential well depth. As one can notice, the Hess-Su potential is a Lennard-Jones potential with a modified attractive term. This modification introduces the fact that the molecules do not align parallel but slightly tilted to each other as it is expected from chiral liquid crystals [1]. The orientation dependence of the inter

molecular interactions is given by:

$$\Psi\left(\hat{\boldsymbol{u}}_i, \hat{\boldsymbol{u}}_j, \hat{\boldsymbol{r}}_{ij}\right) = 5\epsilon_1 P_2\left(\hat{\boldsymbol{u}}_i \cdot \hat{\boldsymbol{u}}_j\right) + 5\epsilon_2\left[P_2\left(\hat{\boldsymbol{r}}_{ij} \cdot \hat{\boldsymbol{u}}_i\right) + P_2\left(\hat{\boldsymbol{r}}_{ij} \cdot \hat{\boldsymbol{u}}_j\right)\right]$$
$$+\epsilon_3\left[\left(\hat{\boldsymbol{u}}_i \times \hat{\boldsymbol{u}}_j\right) \cdot \hat{\boldsymbol{r}}_{ij}\right]\left(\hat{\boldsymbol{u}}_i \cdot \hat{\boldsymbol{u}}_j\right), \tag{2.4}$$

where $P_2(x)$ is the second Legendre polynomial $P_2(x) = \frac{1}{2}\left(3x^2 - 1\right)$, ϵ_1, ϵ_2 the anisotropy parameters and ϵ_3 the chirality parameter. The term proportional to ϵ_3 on the right-hand side of Eq. (2.4) is the simplest pseudo-scalar that induces chiral ordering, according to Memmer [18], The achiral [21, 22] model as well as the chiral one [20, 23] were proved to be capable of correctly reproducing properties of liquid crystals. In order to achieve results comparable to experiments, a confinement of the liquid crystals hast to be introduced. In this model this confinement is given by parallel smooth walls normal to the z-axis and periodic boundary conditions in the other dimensions. In analogy to experimental setups, the walls can be used to manipulate the preferred global orientation of the molecules due to a specific anchoring at that surface. The fluid-substrate interaction for the total energy expression (2.1) is given by:

$$\Phi_{fs}\left(Z, \hat{\boldsymbol{U}}\right) = \sum_{k=1}^{2}\sum_{i=1}^{N}\varphi_{fs}\left(z_i, \hat{\boldsymbol{u}}_i\right) \tag{2.5}$$

with the fluid-substrate interaction:

$$\varphi_{fs}^{(k)} = \epsilon_{fs}\left[a_1\left(\frac{\sigma}{\Delta z_i}\right)^{10} - a_2\frac{\exp\left(-\eta|\Delta z_i|\right)}{|\Delta z_i|}g^{(k)}\left(\hat{\boldsymbol{u}}_i\right)\right]. \tag{2.6}$$

Here ϵ_{fs} determines the depth of the attractive well, $\Delta z_i = z_i \pm s_z/2$ is the distance of the particle from either wall and the sign is chosen accordingly to the interaction with the lower $(k = 1)$ and the upper substrate $(k = 2)$. The dimensionless parameters a_1 and a_2 guarantee that the location of the minimum of the fluid-substrate potential as well as the depth of the attractive well are fixed [20].

When it comes to fluid-substrate interactions, the orientation of the liquid crystal close to the substrate is fixed by the surface. This phenomenon is called anchoring. In this particular setup hybrid anchoring is applied in order to avoid any spurious stress along the simulation box. Even if the dimensions of the simulation box do

not correspond to a multiple half integer of the pitch:

$$g^{(1)} = (\hat{\boldsymbol{u}}_i \cdot \hat{\boldsymbol{e}}_x)^2 \,, \tag{2.7a}$$

$$g^{(2)} = (\hat{\boldsymbol{u}}_i \cdot \hat{\boldsymbol{e}}_x)^2 + (\hat{\boldsymbol{u}}_i \cdot \hat{\boldsymbol{e}}_y)^2 \,, \tag{2.7b}$$

where the unit vector $\hat{\boldsymbol{e}}_\alpha$ is pointing along the x- or y-axis of the Cartesian coordinate system. This makes sure that mesogens located close to the lower substrate will align preferably along the x-axis (2.7a) and mesogens closer to the upper substrate will align their axes parallel to the x-y plane without any preference on the unit circle (2.7b) [20].

2.2.1 Flow

In order to drive the system successfully out of equilibrium, first we have to reconsider the fluid-substrate interactions. In a steadily driven system there is a constant input of energy that must be balanced by some mechanism of energy dissipation. Viscosity is the main form of dissipation in a fluid. Thus, in a driven system it is no longer sufficient to have smooth walls, since there is no friction at the walls. To introduce friction we use walls made of discrete particles. This means that each wall is composed from N_W spherical particles that are arranged according to the (100) configuration of the face-centered cubic (fcc) lattice. In analogy to Gruhn et al. [24], the walls are in registry. This means that corresponding molecules in the two walls are exactly opposite each other. We still employ hybrid anchoring $g^{(k)}(\hat{\boldsymbol{u}}_i)$ in the same fashion and periodic boundary conditions in the x-y plane. This results in the discrete fluid-substrate interaction:

$$\varphi_{fs}^{(k)}(\hat{\boldsymbol{u}}_i, \, \boldsymbol{r}_{ij}) = \epsilon_{fs} \, \rho_0 \, \sigma^2 \left[\frac{2}{5} \left(\frac{\sigma}{r_{ij}} \right)^{10} - \left(\frac{\sigma}{r_{ij}} \right)^4 g^{(k)}(\hat{\boldsymbol{u}}_i) \right] , \tag{2.8}$$

where $\epsilon_{fs} = \frac{5}{3}\epsilon_{ff}$ and $\rho_0\sigma^2 \approx 1.1$ is the areal density of a single layer of substrate particles. The implementation of the flow is done by adding a constant force F_{flow} to each particle in the x-direction. The interplay between particle number, volume of the system and value of F_{flow} determine the steady-state flow profile of the system.

2.3 Methods

In order to extract physical quantities out of the simulations, various techniques can be used. One of the most valuable quantities in a liquid crystal, as presented in Sec. 1.1, is the local orientation of the liquid crystals. A suitable quantitative measure of the local orientational order is provided through the local alignment tensor, which can be defined as

$$\boldsymbol{Q}\left(\boldsymbol{r}\right) \equiv \frac{1}{2\rho\left(\boldsymbol{r}\right)} \sum_{i=1}^{N} \left\langle \left[3\hat{\boldsymbol{u}}_i\left(\boldsymbol{r}_i\right) \otimes \hat{\boldsymbol{u}}_i\left(\boldsymbol{r}_i\right) - \mathbb{1}\right] \delta\left(\boldsymbol{r} - \boldsymbol{r}_i\right)\right\rangle, \qquad (2.9)$$

where $\rho\left(\boldsymbol{r}\right)$ is the local density, $\mathbb{1}$ the unit tensor, $\delta\left(\boldsymbol{r} - \boldsymbol{r}_i\right)$ the Dirac δ-function and $\otimes$ the tensor product. As shown in [1], the local alignment tensor is a real, traceless, symmetric, second-rank tensor, represented by a 3x3 matrix that satisfies the eigenvalue equation:

$$\boldsymbol{Q}\left(\boldsymbol{r}\right)\hat{\boldsymbol{n}}\left(\boldsymbol{r}\right) = \lambda\left(\boldsymbol{r}\right)\hat{\boldsymbol{n}}\left(\boldsymbol{r}\right). \qquad (2.10)$$

Equation (2.10) has three eigenvalues, $\lambda_-(\boldsymbol{r}) < \lambda_0(\boldsymbol{r}) < \lambda_+(\boldsymbol{r})$, and the associated eigenvectors are $\hat{\boldsymbol{n}}_-\left(\boldsymbol{r}\right)$, $\hat{\boldsymbol{n}}_0\left(\boldsymbol{r}\right)$, $\hat{\boldsymbol{n}}_+(\boldsymbol{r})$. The largest local eigenvalue can now be seen as the local nematic order parameter $\lambda(\boldsymbol{r})$ and its eigenvector as the local nematic director $\hat{\boldsymbol{n}}(\boldsymbol{r})$ [20]. Both the local nematic order parameter, as well as the local nematic director give valuable information about the structure of the system. As presented by Schlotthauer et al. [23], defect lines ℓ in the system are being identified by a small value of the local nematic order parameter δ_λ:

$$\ell \equiv \left\{\boldsymbol{r} = (x, y, z)^{\mathrm{T}} \,|\, \lambda\left(\boldsymbol{r}\right) \leq \delta_\lambda\right\}, \qquad (2.11)$$

where the superscript T denotes the transpose of the three dimensional vector $\boldsymbol{r}$. The value of δ_λ is *a priori* unknown and is in practice chosen to enhance the visibility of the defect lines. Furthermore, the rotation of the local nematic director $\hat{\boldsymbol{n}}(\boldsymbol{r})$ is being used together with Eq. (1.1) to measure the pitch in the system.

In order to get an understanding of the positional and orientational dependence of the liquid crystals, the radial distribution function

$$g\left(r\right) = \frac{V}{N^2} \left\langle \sum_i \sum_{j \neq i} \delta\left(r - |\boldsymbol{r}_{ij}|\right) \right\rangle \qquad (2.12)$$

and the pseudoscalar radial orientational pair correlation function

$$S_{221}(r) = -\sqrt{\frac{3}{10}} \langle [(\hat{\boldsymbol{u}}_i \times \hat{\boldsymbol{u}}_j) \cdot \hat{\boldsymbol{r}}_{ij}] (\hat{\boldsymbol{u}}_i \cdot \hat{\boldsymbol{u}}_j) \rangle \tag{2.13}$$

are useful. The average is calculated over all pairs of molecules of a configuration separated by a distance r [25].

The main key dimensionless quantity that is commonly used to describe flowing fluids is the Reynolds number $\mathcal{R}$. The Reynolds number gives a measure of the ratio of inertial forces to viscous forces:

$$\mathcal{R} = \frac{\bar{\rho} v_\infty l}{\eta}, \tag{2.14}$$

where $\bar{\rho}$ is the global density, v_∞ the streaming velocity at steady state, l the characteristic length of the system and η the dynamic viscosity. In this case the typical length scale is the box length in z-direction l_z. In order to calculate the dynamic viscosity η of the system, one has to look at the steady state streaming velocity $v_x(z)$ of a uniform fluid within the weak-flow limit for planar Poiseuille flow, as Todd et al. suggest [26]:

$$v_x(z) = -\frac{\bar{\rho} F_{flow}}{2\eta} \left[z^2 - \frac{l_z}{4} \right], \tag{2.15}$$

where F_{flow} is the external driving force.

3 Computational Details

In order to study the structure formation of chiral liquid crystals, an MD simulation based on CUDA is employed.

3.1 Parameters used

The chiral liquid crystal is studied in a rectangular box at a constant number of particles N, confined between smooth walls in the z-direction and with periodic boundary conditions in the x-y plane, both in the isothermal-isobaric (NPT), as well as in the canonical (NVT) ensemble, using standard molecular dynamics algorithms [16]. While in the NVT ensemble the volume of the simulation box is a constant, it varies in the NPT ensemble, in such a way that the distance between the walls is held fixed, while the box dimensions along the other axes are changing uniformly to match the desired pressure. Dimensionless units are used in this work. In analogy to Melle et al. [20] all simulations were done with fixed anisotropy parameters $\epsilon_1 = 0.04 = -\epsilon_2/2$ which produce mesogens with an aspect ratio of 1.26 [27]. We solve the equations of motion using a velocity-Verlet algorithm with a time step $\delta t = 0.001$.

3.2 Preparation and equilibration

In order to analyze the phase transitions, we first carried out a series of careful equilibrations in the isothermal-isobaric ensemble. During this series the chirality parameter was being increased from $\epsilon_3 = 0.00$ (achiral) to $\epsilon_3 = 0.98$ in steps of $\Delta\epsilon_3 = 0.02$ while pressure, temperature and number of particles were fixed at $P = 1.8$, $T = 0.94$ and $N = 40\,000$, respectively. This choice of equilibrating the system from an achiral state into a chiral one minimizes the impact of hysteresis. Furthermore the isothermal-isobaric ensemble allows us to find the equilibrium density and, together with hybrid anchoring as presented in Eq. (2.7), the equilibrium

14

pitch can be reached during the equilibration process since these values are not known *a priori* for the system. Each simulation was run for 400 000 time steps.

To explore the pressure-temperature dependency of the system, in the next step the temperature is reduced from $T = 0.94$ to $T = 0.86$ in steps of $\Delta T = 0.02$, for fixed pressure $P = 1.8$ and for fixed selected values of chirality $\epsilon_3 = \{0.02, 0.08, 0.14, 0.18, 0.28, 0.38, 0.48, 0.58, 0.68, 0.78, 0.88, 0.98\}$. After the equilibration of these temperature-chirality pairs, each set underwent a reduction of pressure from $P = 1.8$ to $P = 1.0$ in steps of $\Delta P = 0.2$ The process of preparing and equilibrating the system is schematically visualized in Fig. 3.1.
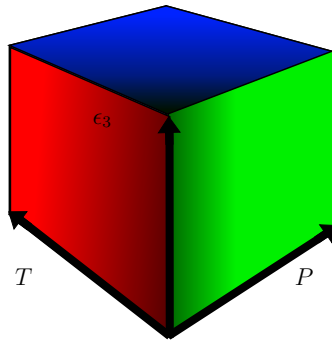
Figure 3.1: Schematic representation of the equilibration process. The color gradient indicates the transition through the phase space, starting from the origin of the box.

3.3 NPT ensemble

Now that the simulations for a various range of parameters are equilibrated, we can measure the pitch along the z-axis. This axis is naturally parallel to the helical axis and is not directly affected by the changing volume of the simulation box. The pitch along the z-axis can be calculated from the local nematic director $n_\alpha(z)$, with $\alpha = x, y$. In order to get significant measurements, the data were averaged over 500 000 time steps. The average global number density $\bar{\rho}(\boldsymbol{r})$ was averaged over the last 100 000 time steps. For the sampling process a virtual sampling box was chosen with dimensions smaller than the real simulation box for all times. This makes sure that data were collected from an area that is not directly affected by the changing wall sizes. The sampling box itself was then binned into boxes with a size of $(0.3\,\sigma)^3$

in order to calculate the local director and local nematic order parameter in each small bin via Eq. (2.9).

3.4 NVT ensemble

Because we want to study both the equilibrium properties and the dynamics of the liquid crystal system, it is desirable to remove the perturbations to the dynamics caused by the barostat. Thus, to reproduce the results from the NPT simulations in an NVT ensemble, the calculations of the average pitch $\bar{p}(z)$ and the average density $\bar{\rho}(\boldsymbol{r})$ are used to construct a simulation box whose side-lengths are half-integer multiples of the average pitch and with a number of particles that matches the equilibrium density at those specific values of T, P and ϵ_3. Furthermore, the particle number varies between 19 000 and 43 000 particles for the NVT simulations. Hereby one has to keep in mind that the average pressure $\langle P \rangle$ itself is an intensive thermodynamic variable and cannot be explicitly controlled in the NVT ensemble, but results directly from the Helmholtz free energy $F(N, V, T)$:

$$\langle P \rangle = -\frac{\partial F}{\partial V}. \tag{3.1}$$

In the following the pressure reported in the results of NVT simulations is the corresponding NPT simulation pressure and not the explicitly measured one (see Ch. 5). The simulations were done for chosen representative values as shown in

ϵ_3	P	T
0.18	1.0	0.86
0.18	1.4	0.90
0.18	1.8	0.94
0.48	1.0	0.86
0.48	1.4	0.90
0.48	1.8	0.94
0.78	1.0	0.86
0.78	1.4	0.90
0.78	1.8	0.94

Table 3.1: Overview of values from NPT simulations used to construct corresponding NVT simulations.

Table 3.1. In contrast to the NPT simulations the NVT simulations did not undergo

the tedious process of equilibration. Instead each simulation was started from a random configuration of the molecules since the equilibrium conditions are now known. Both the equilibration as well as the sampling of the data were done for 500 000 time steps each. For the sampling process this time the whole system was divided into bins with a size of $(0.3\,\sigma)^3$.

3.5 NVT flow

To investigate the influence of flow on the system, the selected simulation for values of $\epsilon_3 = 0.78$, $T = 0.94$ and $P = 1.8$ with $N = 19209$ particles is equilibrated for 500 000 time steps in an NVT ensemble with discrete walls. After the equilibration, three different flow forces $F_{flow} = 0.2$, 0.4 and 0.8 were used. To calculate a velocity profile, the x-y plane is divided into 320 slices, so one can display the x-component of the velocity in dependency of the z-position $v_x(z)$. In order to monitor the time evolution of the velocity profile, this is done every 100 000 time steps for 500 000 time steps in total. To have a good estimate of the steady-state velocity v_∞, the average velocity over all particles for $t = 500\,000$ is calculated. Since we drive our system out of equilibrium, we now have do differentiate between the true particle velocities and the local streaming velocity of the fluid at the particle position. This has to be taken into account to calculate friction, in order to conserve energy and momentum of the system. Especially sensitive is the thermostat. In order to preserve the hydrodynamic properties of the system, a Galilean invariant thermostat has to be introduced, first presented by Stoyanov and Groot [28], which is a combination of pairwise Nosé-Hoover and Lowe-Andersen thermostat.

4 Results

4.1 NPT pitch

The pitch is a highly sensitive physical quantity of chiral systems. It depends primarily on the chirality ϵ_3 of the molecules, as presented in Eq. (1.2). But also the temperature, pressure and the molecular density influence the pitch of the system. Since the molecular density is not known *a priori* in the NPT ensemble, we will put our focus onto the dependencies of the pitch on chirality, pressure and temperature. For all parameters the pitch was calculated in the following way.

The system was divided into a three dimensional grid as described in Sec. 3.3. For the measurement of the pitch, only the x and y components of the local nematic director in z direction are of interest, while the remaining x-y plane is used to average the local nematic director and the local nematic order parameter $\bar{\lambda}(z)$. This results in two components of the director $\bar{n}_\alpha(z)$, with $\alpha = x, y$ and one constant zero component $\bar{n}_z(z)$ as it is shown in Fig. 4.1 and Fig. 4.2. The pitch was then obtained via fitting Eq. (1.1) with a nonlinear least-squares Marquardt-Levenberg algorithm to the data. Furthermore, the local nematic order parameter is being used to distinguish between a helical phase and a blue phase. This is possible since both phases exhibit a characteristic pitch, yet the helical phase is highly ordered. This results in an overall high nematic order parameter for the helical phase, whereas the blue phase is isotropic in all directions [1] which is accompanied with a low nematic order parameter. This is shown in Fig. 4.1 and Fig. 4.2. In both figures the average nematic director follows perfectly the theoretical behavior as presented in Eq. (1.1). Yet the nematic order parameter for Fig. 4.1 is overall high. This indicates a helical phase. Figure 4.2 has instead a low nematic order parameter. This indicates a blue phase.

In order to get a more vivid image of the simulated system, Fig. 4.3 shows a snapshot of a typical helical phase of the system and Fig. 4.4 of a typical blue phase. One can notice a strong symmetry in the paper plane. This structure can
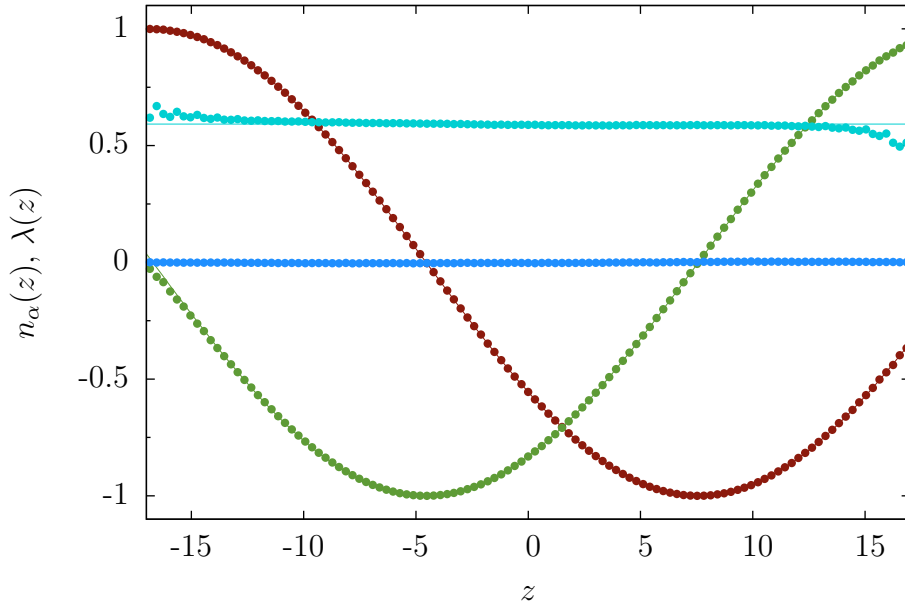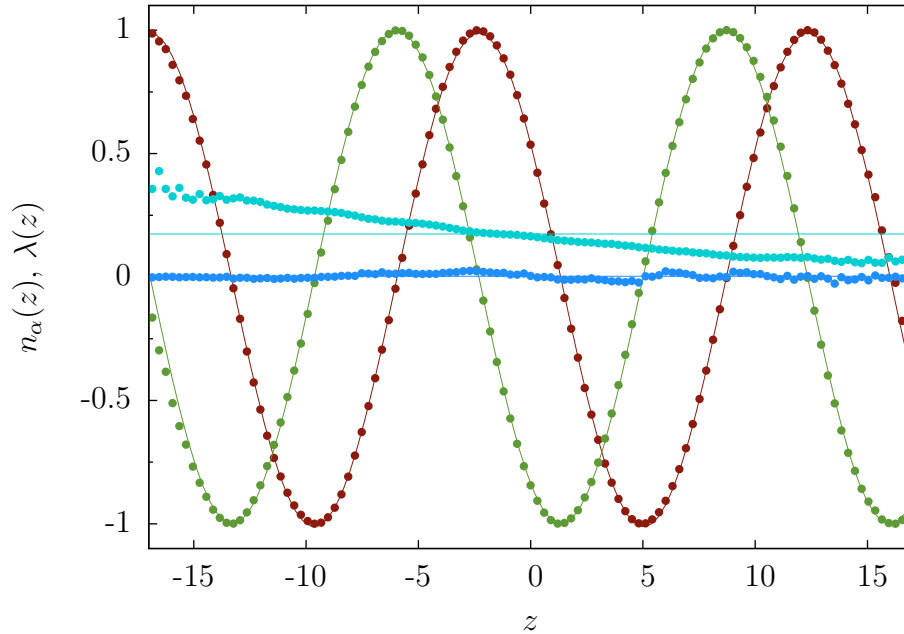
Figure 4.1: Plots of the three components of the average nematic director $\bar{n}_\alpha(z)$, with $\alpha = x$ (red), y (green), z (blue) and the average nematic order parameter $\bar{\lambda}(z)$ (light blue) along the z-axis with the corresponding least-square fit (solid line). The plot was made for constant values of $\epsilon_3 = 0.08$, $p = 1.8$, $T = 0.94$, $N = 40\,000$. The nematic order parameter indicates a helical phase.

be identified as double-twist helices arranged in an sc lattice, which means, in other words, that the presented phase has the form of a BP II. Yet, as one can notice in Fig. 4.4, the double-helix tubes are not perfectly aligned along the line of vision. More regarding that topic can be found in Ch. 5. This analysis has been repeated for the different values of ϵ_3 as presented in Sec. 3.2, while the pressure and temperature are held fixed at $P = 1.8$ and $T = 0.94$. Figure 4.5 shows that the pitch is inversely proportional to the chiral coupling constant ϵ_3, as shown in [20]. We repeated that procedure for all temperature and pressure pairs, as presented in Sec. 3.2 and could verify the same pitch-chirality dependency for all parameters (see Fig. 4.6). Table 4.1 shows the temperature and pressure dependency of the fitting parameters.

Furthermore, we investigated the dependency of temperature and the dependency of pressure on the pitch. In order to do so, this time the pitch was plotted against the pressure and chirality, or against the temperature and chirality. The results are shown in Fig. 4.7(a) and Fig. 4.7(b). For a small pitch, or a high chiral coupling constant ϵ_3, the dependency between chirality and pressure and temperature can

Figure 4.2: Plots of the three components of the average nematic director $\bar{n}_\alpha(z)$, with $\alpha = x$ (red), y (green), z (blue) and the average nematic order parameter $\bar{\lambda}(z)$ (light blue) along the z-axis with the corresponding reduced chi-square fit (solid line). The plot was made for constant values of $\epsilon_3 = 0.48$, $p = 1.8$, $T = 0.94$, $N = 40\,000$. The nematic order parameter indicates a blue phase.

be seen as nearly constant. This changes with an increasing pitch for the pressure dependency, as it can be seen in Fig. 4.7(a). For a small value of $\epsilon_3 = 0.02$ the pitch is proportional to the temperature. These complex dependencies interfere with the idea of a simple master equation that takes care of the interplay between chirality, temperature and pressure in a correct way.

(a)   **(b)**
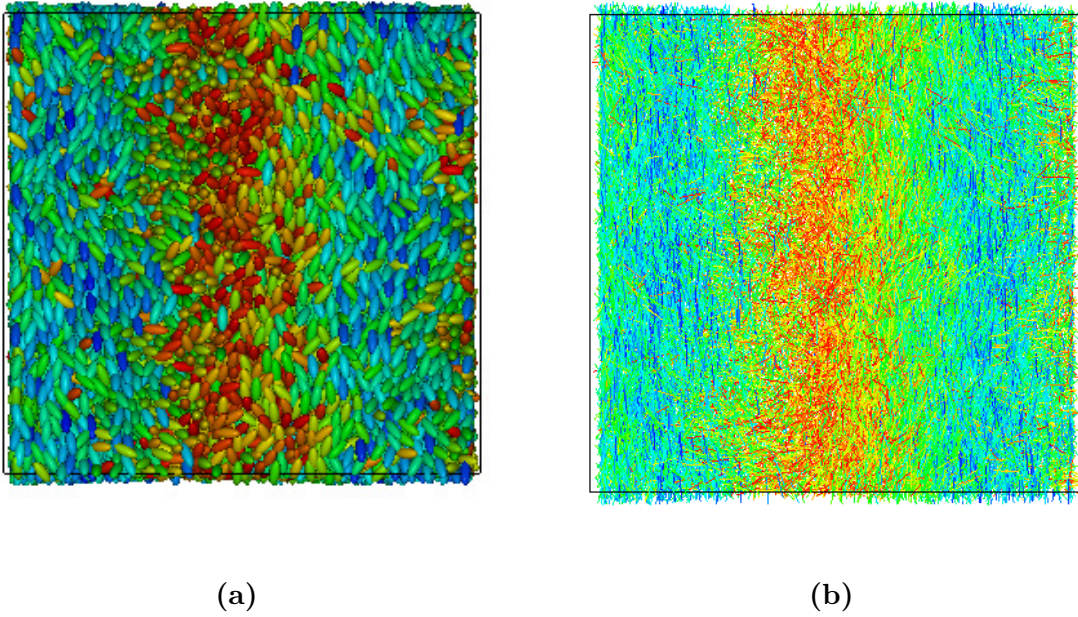
Figure 4.3: Snapshot of a configuration with $\epsilon_3 = 0.08$, $P = 1.8$, $T = 0.94$ in the NPT ensemble. Shown is the x-y plane. The helical axis is parallel to the z-axis. The color code shows molecules pointing in the x-direction in blue and those whose orientation deviates from that in other colors. Since the molecules are head-tail symmetric, the orientation can maximally deviate by 90° (red). The helical phase evolves cleanly from the bottom wall (left side) to the top wall (right side). In order to enhance visibility, the aspect ratio of the mesogens in (a) is exaggerated. To make the structure more visible this visualization is dropped in (b).

(a) **(b)**
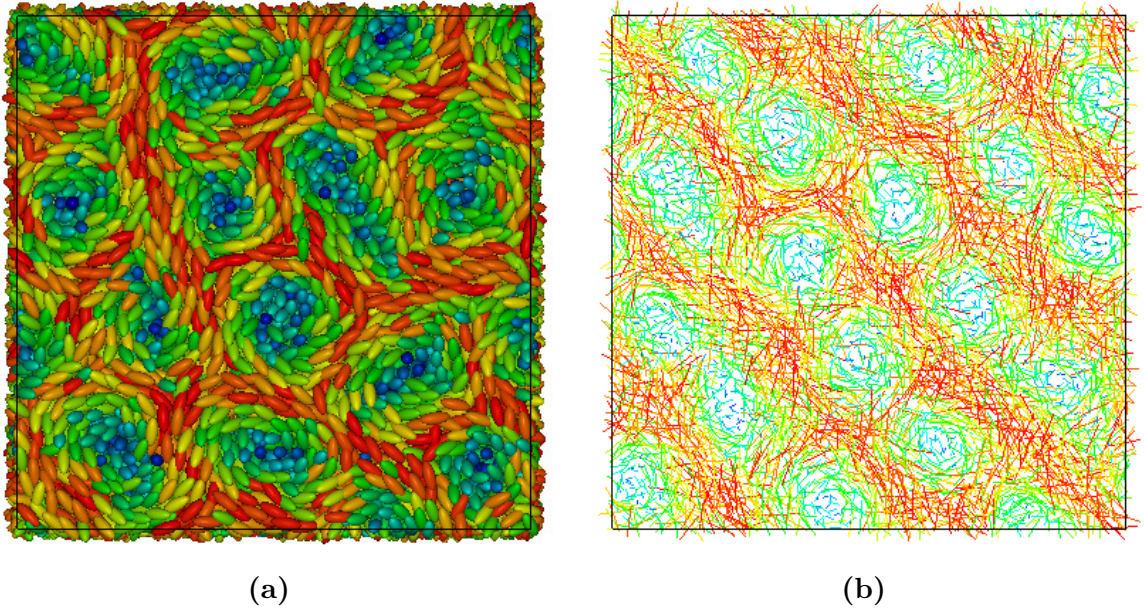
Figure 4.4: Snapshot of a configuration with $\epsilon_3 = 0.48$, $P = 1.8$, $T = 0.94$ in the NPT ensemble. The color code denotes mesogens oriented along the line of vision in blue whereas mesogens that are lying in the paper plane are colored in red. In order to enhance the visibility the aspect ratio is exaggerated in (a). To make the structure more visible, the 3D visualization in (b) is dropped. While (a) is a snapshot that shows the view of the top layer of mesogens, (b) is chosen to show a layer at the bottom wall. As one can notice, the double-helix tubes are not perfectly parallel to the line of vision.
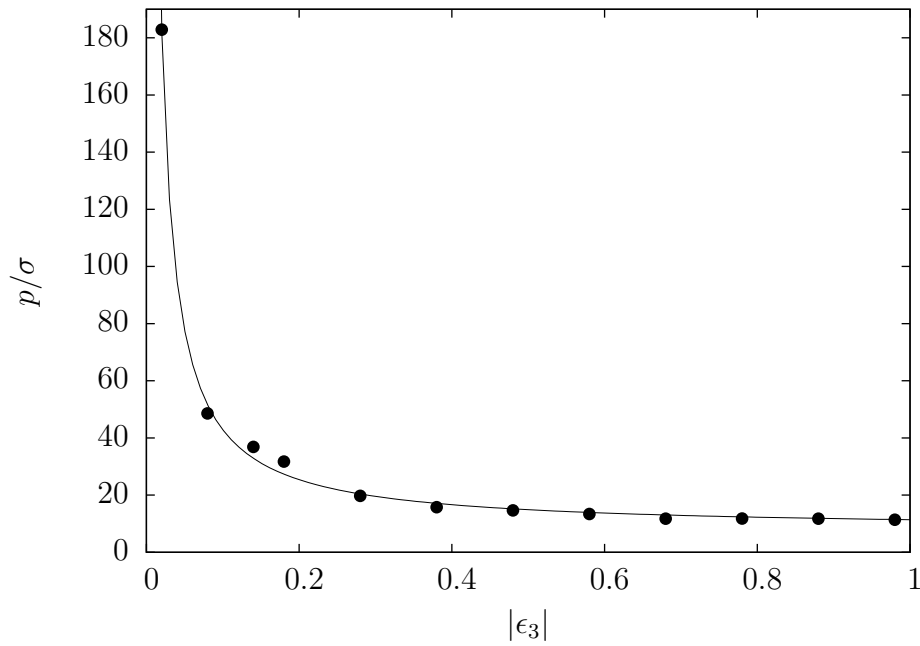
Figure 4.5: Plot of the dimensionless pitch p/σ as a function of the chirality ϵ_3. Data obtained for constant pressure $P = 1.8$ and temperature $T = 0.94$ with a least-square fit (solid line) of $p/\sigma = a/|\epsilon_3| + b$, with $a = 3.50$ and $b = 7.50$. The region $\epsilon_3 \in [0.14, 0.20]$ is the transition region from the helical phase into the blue phase. This explains the slight deviation from the theoretical prediction.

(a) $P = 1.0$

(b) $P = 1.2$

(c) $P = 1.4$

(d) $P = 1.6$

(e) $P = 1.8$
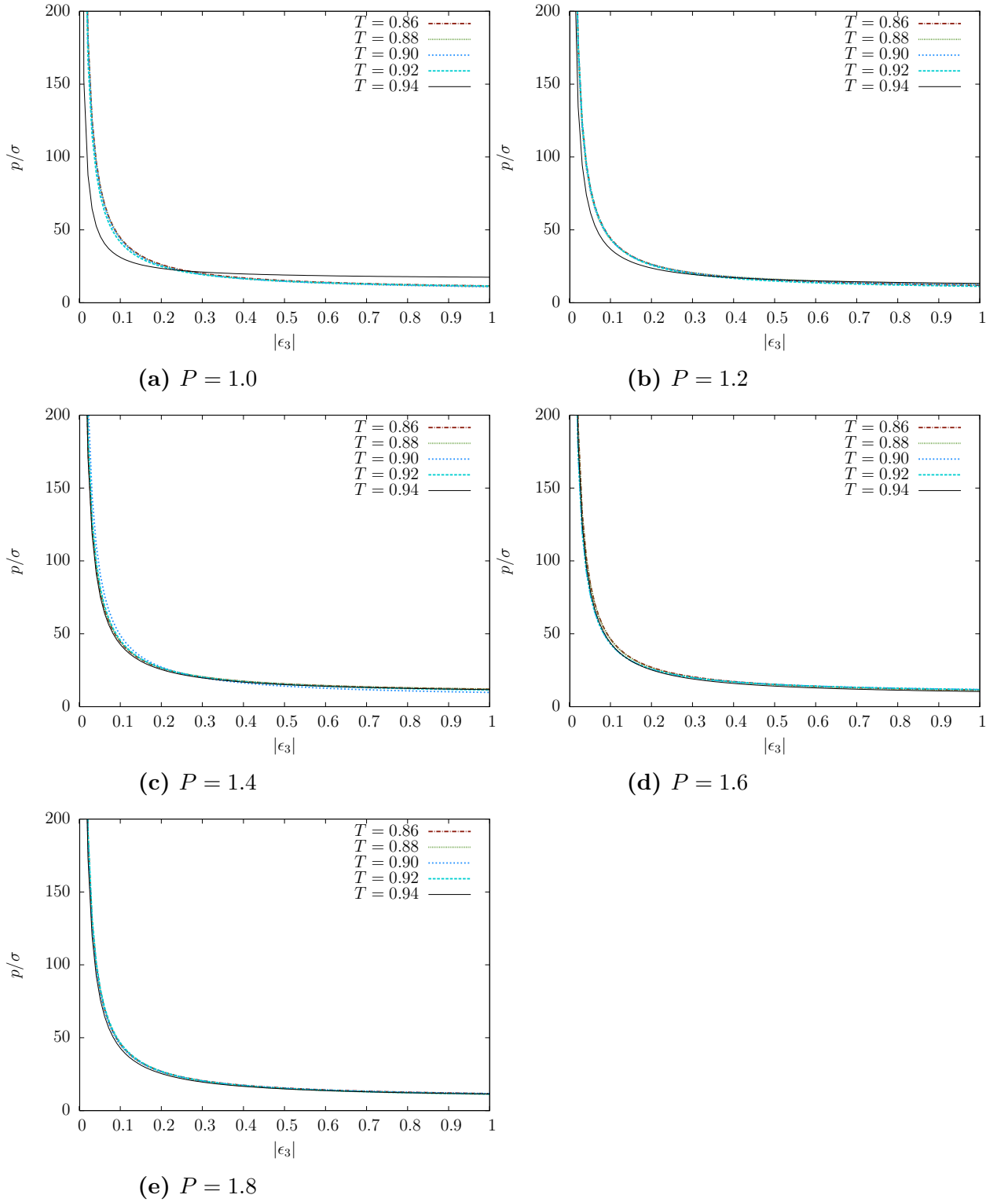
Figure 4.6: Plot of the dimensionless pitch p/σ as a function of chirality ϵ_3 for different temperatures at constant pressures. In analogy to Fig. 4.5 the function $p = a/\epsilon + b$ was fitted to the data with a least-square fit. The final fit parameters a and b are presented in Tab. 4.1. The influence of the temperature on the pitch decreases significantly with increasing pressure.

	$P = 1.0$	$P = 1.2$	$P = 1.4$	$P = 1.6$	$P = 1.8$
$T = 0.86$	$a = 3.67, b = 7.88$	$a = 3.59, b = 8.38$	$a = 3.60, b = 8.38$	$a = 3.91, b = 7.48$	$a = 3.80, b = 7.89$
$T = 0.88$	$a = 3.68, b = 7.39$	$a = 3.42, b = 9.33$	$a = 3.61, b = 8.54$	$a = 3.90, b = 7.17$	$a = 3.80, b = 7.51$
$T = 0.90$	$a = 3.63, b = 7.40$	$a = 3.47, b = 8.92$	$a = 4.36, b = 5.41$	$a = 3.47, b = 8.34$	$a = 3.71, b = 7.99$
$T = 0.92$	$a = 3.34, b = 8.16$	$a = 3.64, b = 7.63$	$a = 3.79, b = 7.67$	$a = 3.50, b = 8.27$	$a = 3.92, b = 7.40$
$T = 0.94$	$a = 1.51, b = 16.02$	$a = 2.62, b = 10.68$	$a = 3.44, b = 8.28$	$a = 3.70, b = 6.71$	$a = 3.50, b = 7.90$

Table 4.1: Fit parameter of least-square fit of the dimensionless pitch $p/\sigma = a/\epsilon_3 + b$, as presented in Fig. 4.6.
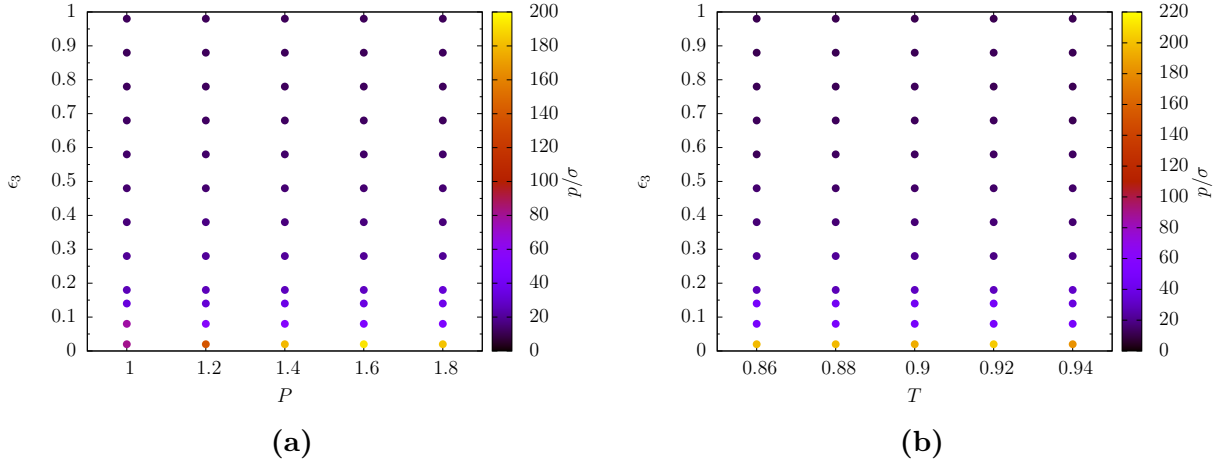
Figure 4.7: Plots show the dependency of pitch p/σ against pressure P for constant temperature $T = 0.94$ (a) and against temperature T for constant pressure $P = 1.8$ (b) for different values of ϵ_3. The color code denotes the measured pitch p/σ. As seen in Figure (a), the pitch increases with increasing temperature for small values of ϵ_3. Whereas the pitch can be seen as constant for higher values of ϵ_3. In Fig. (b) the pitch can be seen as constant for $P = 1.8$ regarding the temperature T and is inverse proportional to the chirality.

4.2 NVT disclination lines

Disclination lines are an important method for describing the structure of liquid crystals. One can directly extrapolate the structure of the system from disclination lines and vice versa. In complete analogy to Schlotthauer et al. [23], disclination lines are being visualized by plotting only areas that have a small nematic order parameter δ_λ. Its value is typically in the range $0.15 \leq \delta_\lambda \leq 0.25$. In this work the upper limit was exceeded in rare occasions in order to enhance the visibility of the disclination lines. The color code shall help to visualize the 3D disclination lines, as it is presented in Fig. 4.8. Hereby each specific point of the defect lines ℓ is assigned

a different color. As Fig. 4.9 shows, different complex networks of disclination lines

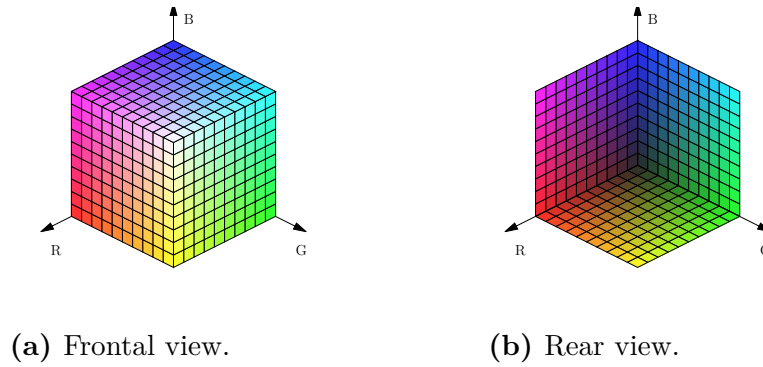**(a)** Frontal view.

(b) Rear view.

Figure 4.8: Cube of unit-length where the spatial variation of color illustrates the position of the disclination lines in a 3D space.

are being formed under different conditions. The most common structure here has tetrahedral arranged lines. This kind of symmetry is expected for a BP II [29]. With increasing chirality and hence decreasing pitch, the mesh of the disclination lines becomes more subtle.

However, the disclination network for low values of ϵ_3 is qualitatively different from the others. As temperature and pressure increases (Fig. 4.9(a) - Fig. 4.9(c)) the structure changes from a tangled one, into a tetrahedral. This is an indicator for a transition from BP III into BP II.
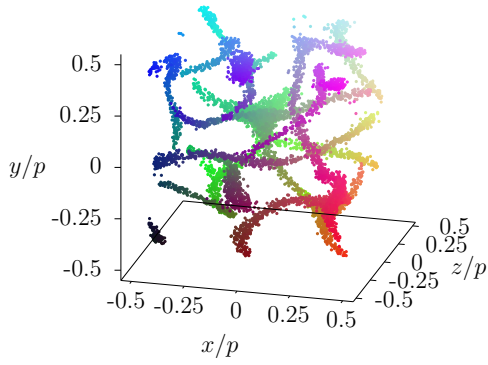
(a) Disclination lines ℓ for $\epsilon_3 = 0.18$, $P = 1.0$, $T = 0.86$.
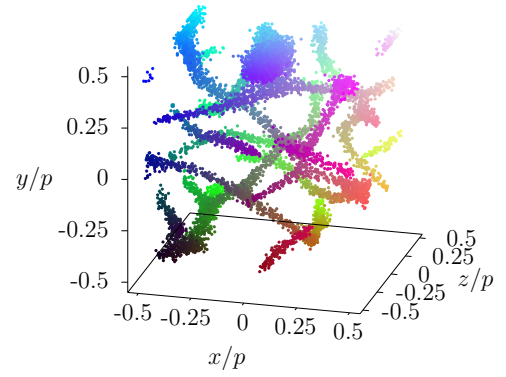
(b) Disclination lines ℓ for $\epsilon_3 = 0.18$, $P = 1.4$, $T = 0.90$.
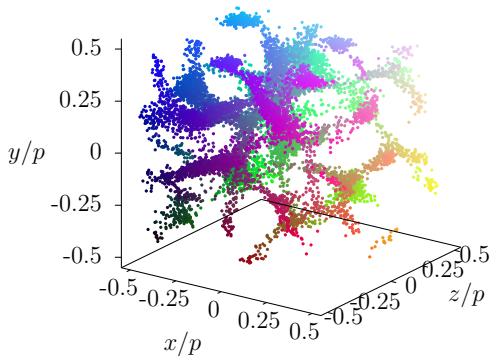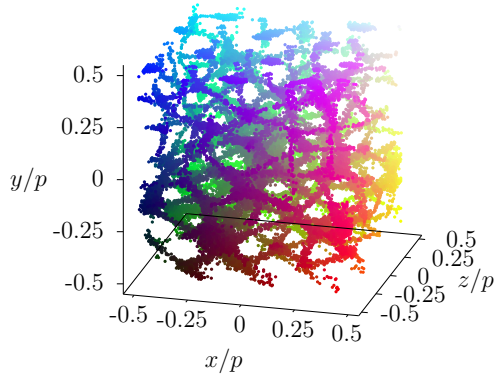
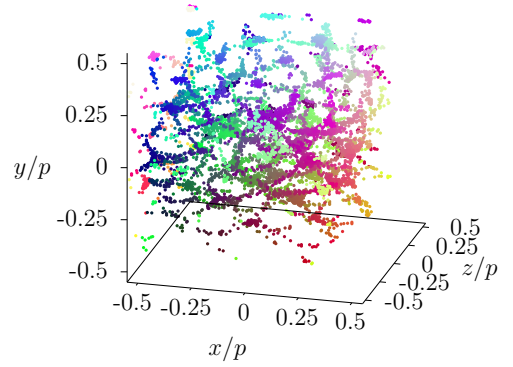**(c)** Disclination lines ℓ for $\epsilon_3 = 0.18$, $P = 1.8$, $T = 0.94$.
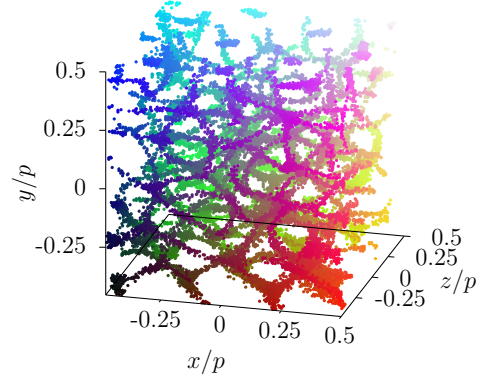
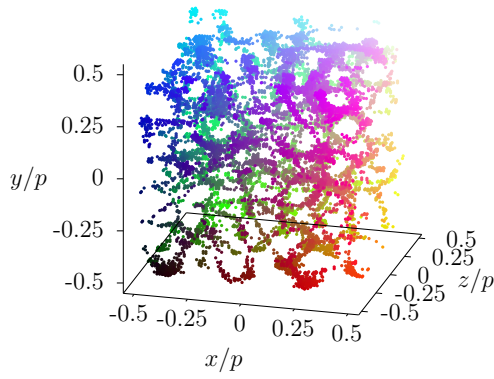**(d)** Disclination lines ℓ for $\epsilon_3 = 0.48$, $P = 1.0$, $T = 0.86$.

4 Results

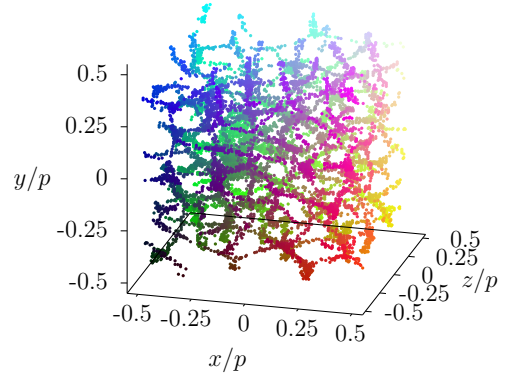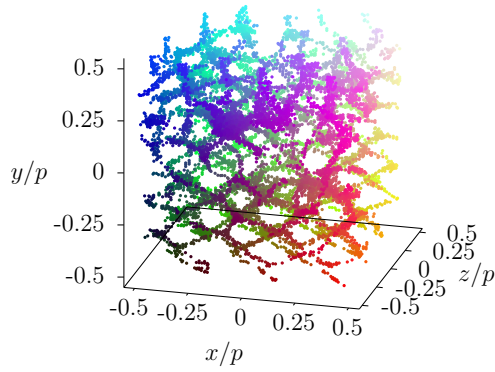**(e)** Disclination lines ℓ for $\epsilon_3 = 0.48$, $P = 1.4$, $T = 0.90$.

(f) Disclination lines ℓ for $\epsilon_3 = 0.48$, $P = 1.8$, $T = 0.94$.

(g) Disclination lines ℓ for $\epsilon_3 = 0.78$, $P = 1.0$, $T = 0.86$.

(h) Disclination lines ℓ for $\epsilon_3 = 0.78$, $P = 1.4$, $T = 0.90$.

(i) Disclination lines ℓ for $\epsilon_3 = 0.78$, $P = 1.8$, $T = 0.94$.

Figure 4.9: Visualizations of disclination lines ℓ for different chiral coupling constants ϵ_3, temperatures T and pressures P.

4.3 NVT radial orientation functions

Radial orientation functions are an important method to characterize local order. While there are numerous different radial orientation functions, for this work it is sufficient to concentrate on the radial distribution function (2.12) and the pseudo-scalar radial orientational pair correlation function (2.13). Figures 4.10 - 4.18 show the radial distribution as well as the orientational pair correlation function for selected system parameters. As one can notice, the radial distribution functions show the typical structure characteristics of a liquid. While we have a strong positional correlation in the nearest neighbor regime, this correlation decreases towards one for larger distances r. Although $g(r)$ does not reach exactly one for large distances, the function converges slightly below one. This occurs due to the walls in z-direction. The volume close to the walls is being slightly overestimated which then results in a too big a normalization value in the numerator, which leads to a correlation slightly lower than one for large distances. Furthermore one can notice that the value of the first peak increases with increasing chirality. With higher chirality higher filling fraction values can be reached in the nearest neighbor region, since the particles are stronger tilted against each other.

The radial orientational pair correlation functions $S_{221}(r)$ for selected system parameters are also presented. The pseudo scalar radial orientational pair correlation functions are used to quantify helical superstructures. $S_{221}(r)$ is significantly nonzero at short separations identifying chiral correlations. Due to the chosen handedness of the mesogens, the peak has all negative values in the nearest neighbor regime and is maintained over large distances. This indicates helical superstructures [25]. Yet the correlation converges to values close to zero for large distances. This is in perfect agreement with the fact that blue phases are isotropic in all directions and yet show strong local order. In analogy to the radial distribution function these characteristics amplify with increasing chirality which indicates increasing distinctiveness of the blue phase.

To sum up, the radial orientation functions show that the system is liquid although it exhibits strong local orientational order. Furthermore, it is shown that with increasing chirality the characteristics of the blue phase are being excelled. With other words, with higher chirality one goes deeper into the blue phase. Although the disclination lines for low chiralities (see Fig. 4.9(a)) look qualitatively different from those of a BP II, no significant difference in the radial orientation functions
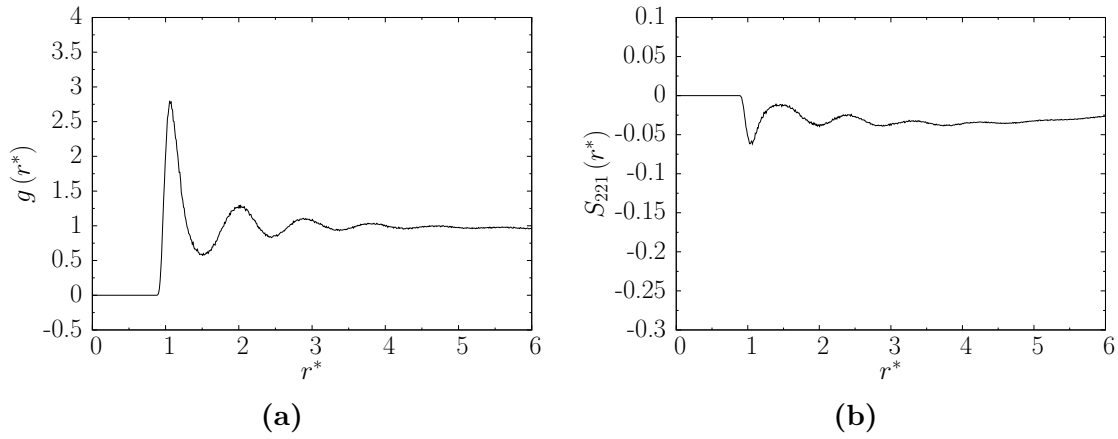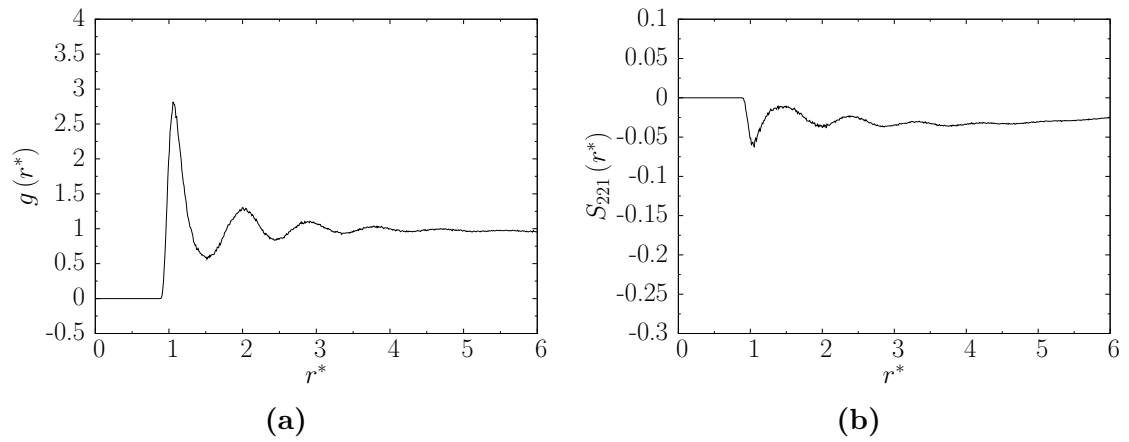
Figure 4.10: Dependence of the radial pair correlation function and radial orientational pair correlation function on the intermolecular separation r^* for $\epsilon_3 = 0.18$, $P = 1.0$, $T = 0.86$.

(see Fig. 4.10) can be found. Hence no clear verification of the existence of a BP III for these parameters is possible.

In contrast to the other plots of the radial orientation functions, Figure 4.16 has a rather bumpy progression. This indicates a transition to a solid state. With other words, for these specific parameters the system is almost frozen.

Figure 4.11: Dependence of the radial pair correlation function and radial orientational pair correlation function on the intermolecular separation r^* for $\epsilon_3 = 0.18$, $P = 1.4$, $T = 0.90$.
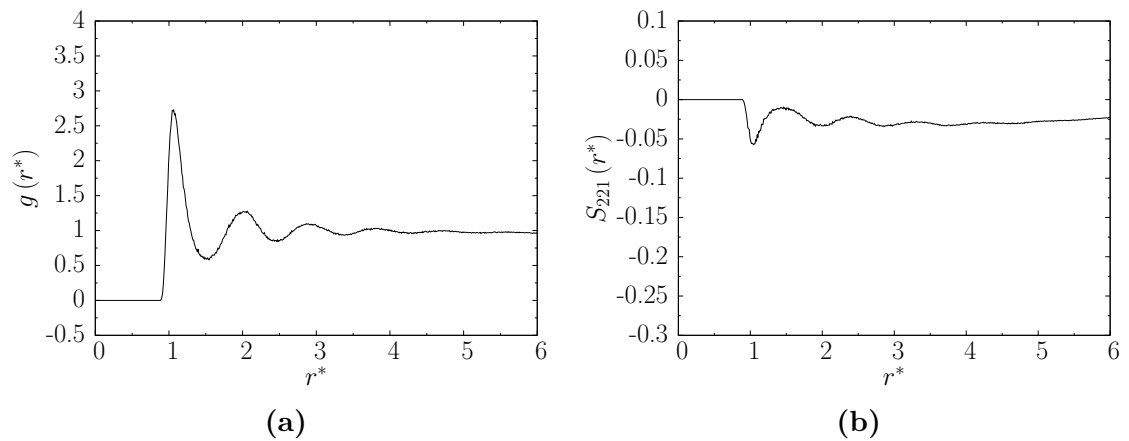

Figure 4.12: Dependence of the radial pair correlation function and radial orientational pair correlation function on the intermolecular separation r^* for $\epsilon_3 = 0.18$, $P = 1.8$, $T = 0.94$.
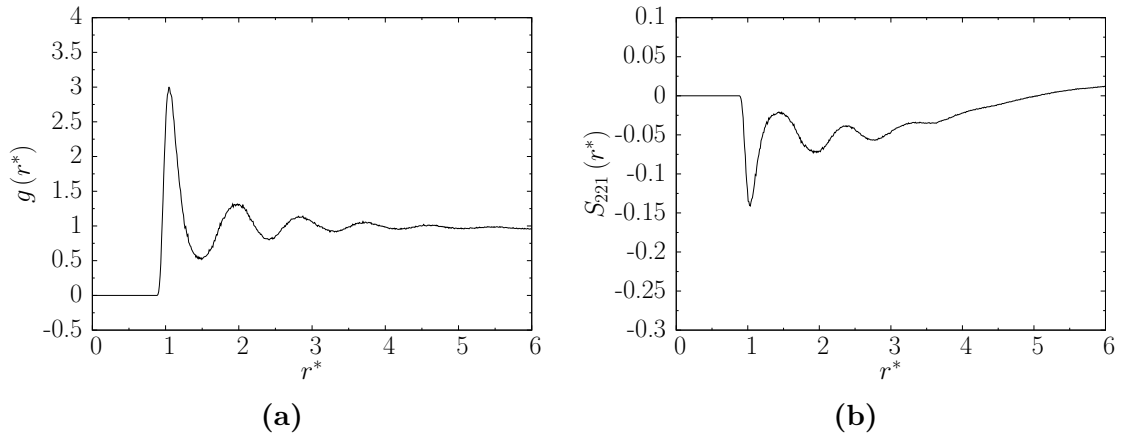
(a)   **(b)**

Figure 4.13: Dependence of the radial pair correlation function and radial orientational pair correlation function on the intermolecular separation r^* for $\epsilon_3 = 0.48$, $P = 1.0$, $T = 0.86$.
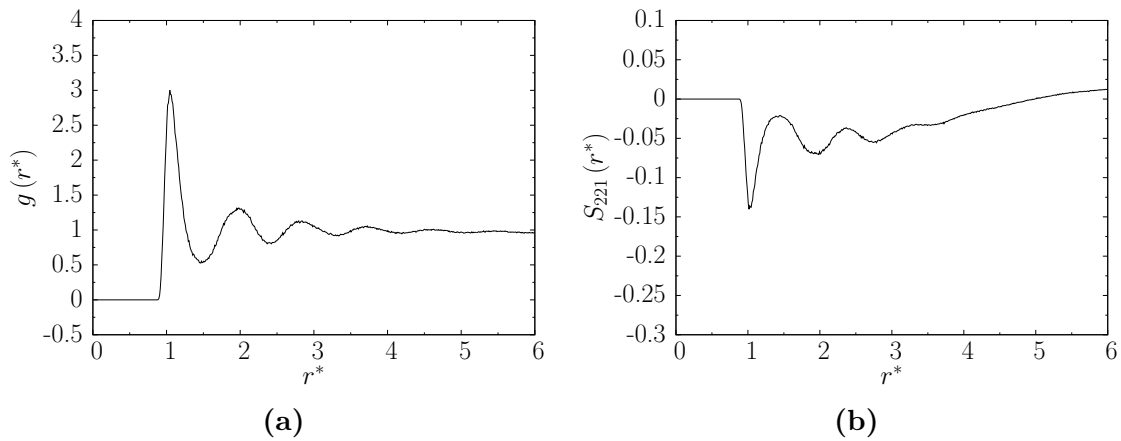

(a)   **(b)**

Figure 4.14: Dependence of the radial pair correlation function and radial orientational pair correlation function on the intermolecular separation r^* for $\epsilon_3 = 0.48$, $P = 1.4$, $T = 0.90$.

(a)   **(b)**

Figure 4.15: Dependence of the radial pair correlation function and radial orientational pair correlation function on the intermolecular separation r^* for $\epsilon_3 = 0.48$, $P = 1.8$, $T = 0.94$.
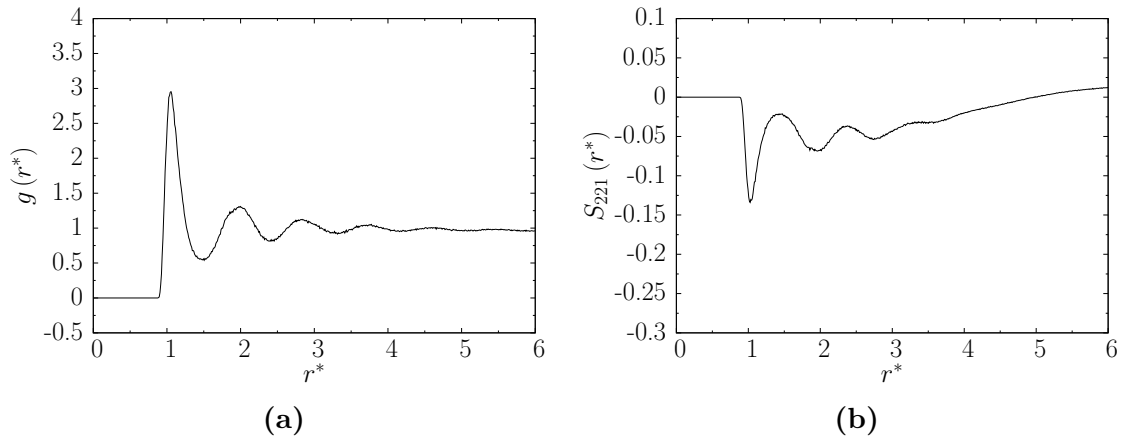

(a)   **(b)**

Figure 4.16: Dependence of the radial pair correlation function and radial orientational pair correlation function on the intermolecular separation r^* for $\epsilon_3 = 0.78$, $P = 1.0$, $T = 0.86$. Since the graph is rather rough, we can assume that the system is close to be in the solid state.
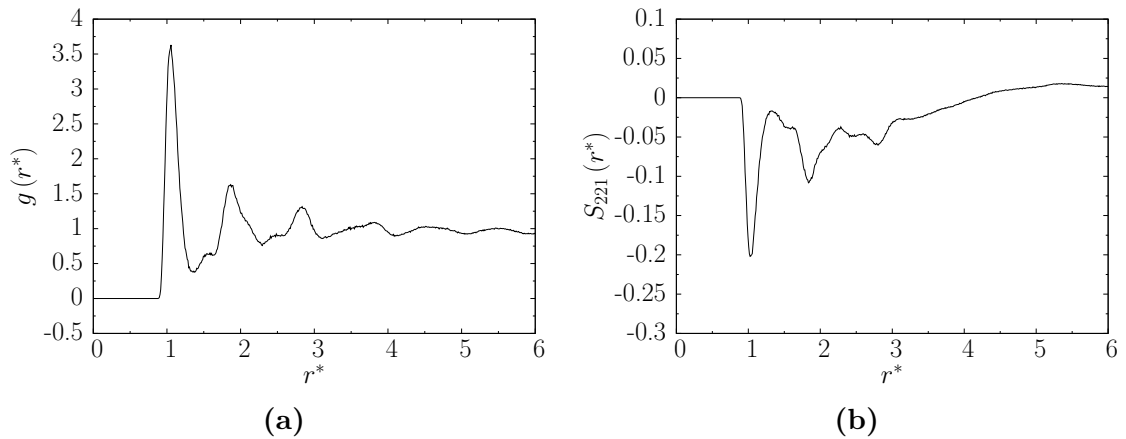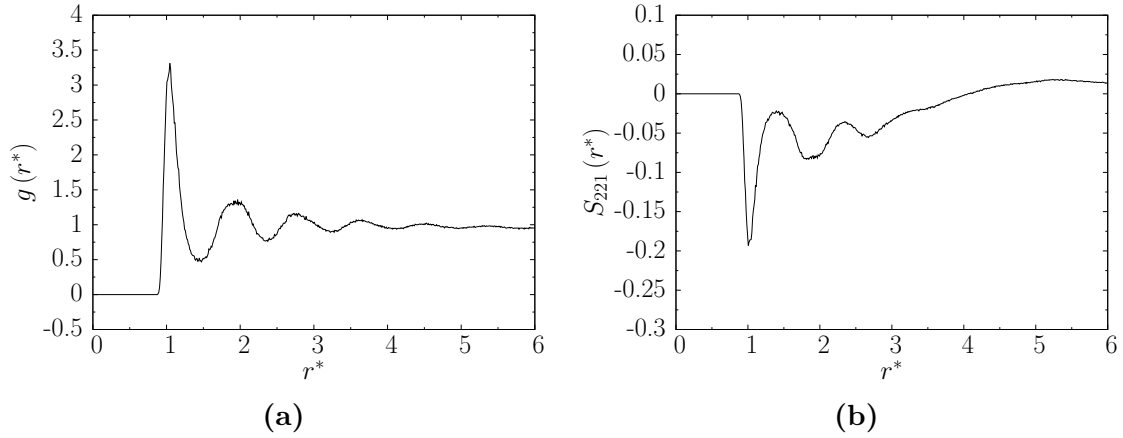
Figure 4.17: Dependence of the radial pair correlation function and radial orientational pair correlation function on the intermolecular separation r^* for $\epsilon_3 = 0.78$, $P = 1.4$, $T = 0.90$.
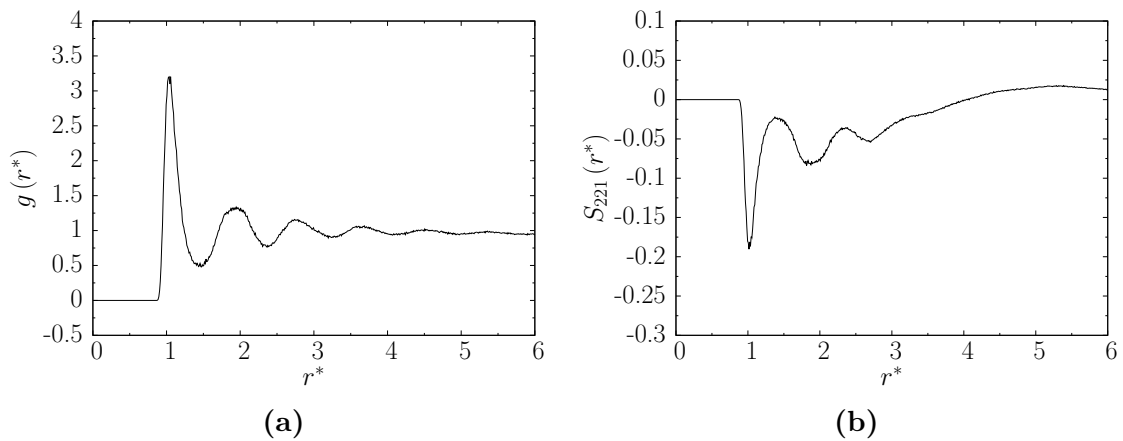

Figure 4.18: Dependence of the radial pair correlation function and radial orientational pair correlation function on the intermolecular separation r^* for $\epsilon_3 = 0.78$, $P = 1.8$, $T = 0.94$.

4.4 Phase diagram

Based on the characterization of the structure seen in the previous sections, a phase diagram in the NPT ensemble can be produced to get an overview of the highly complex interplay between pressure, temperature and chirality. The presented phase diagrams shall give a rough overview over the dependencies.

Figure 4.19 shows the behavior of the system for a small chirality $\epsilon_3 = 0.02$. The system is very sensitive to temperature and pressure changes. A blue phase has not been observed in that region. For slightly increased chirality ($\epsilon_3 = 0.08$), we find a phase diagram that contains the phase transitions that Fig. 1.4 shows. As Fig. 4.20 shows, we observed the phase transition from a helical phase into a blue phase into an isotropic phase for $P = 1.2$ with increasing temperature. Furthermore, Fig. 4.20 shows that this transition can also happen if we decrease the pressure from $P = 1.8$ to $P = 1.0$ for constant temperature $T = 0.94$. This observation emphasizes the complex interplay between temperature and pressure. For increased chirality, we observed blue phases over a wide range of temperature and pressure, as Fig 4.21 presents. From that we can derive that the stability of blue phases increases drastically with the chirality.
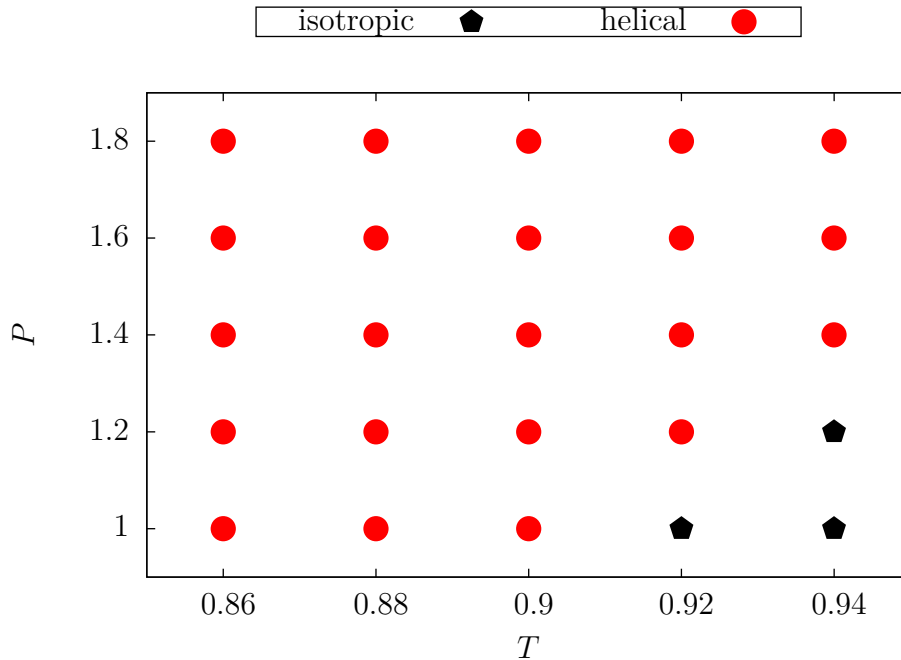
Figure 4.19: Temperature-Pressure phase diagram for a constant chirality of $\epsilon_3 = 0.02$. The transition between an isotropic phase and a helical phase depends highly on the temperature and pressure for small chiralities.
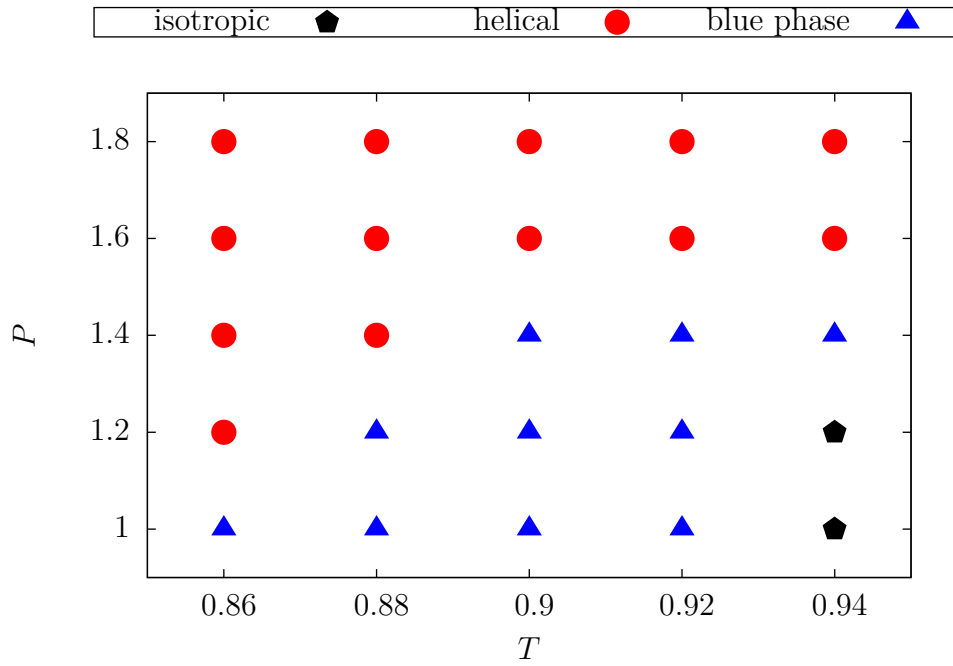
Figure 4.20: Temperature-Pressure phase diagram for a constant chirality of $\epsilon_3 = 0.08$. Phase transitions from helical into blue phase into isotropic are shown for increasing temperature as well as for decreasing pressure.

(a) P=1.8

(b) P=1.6
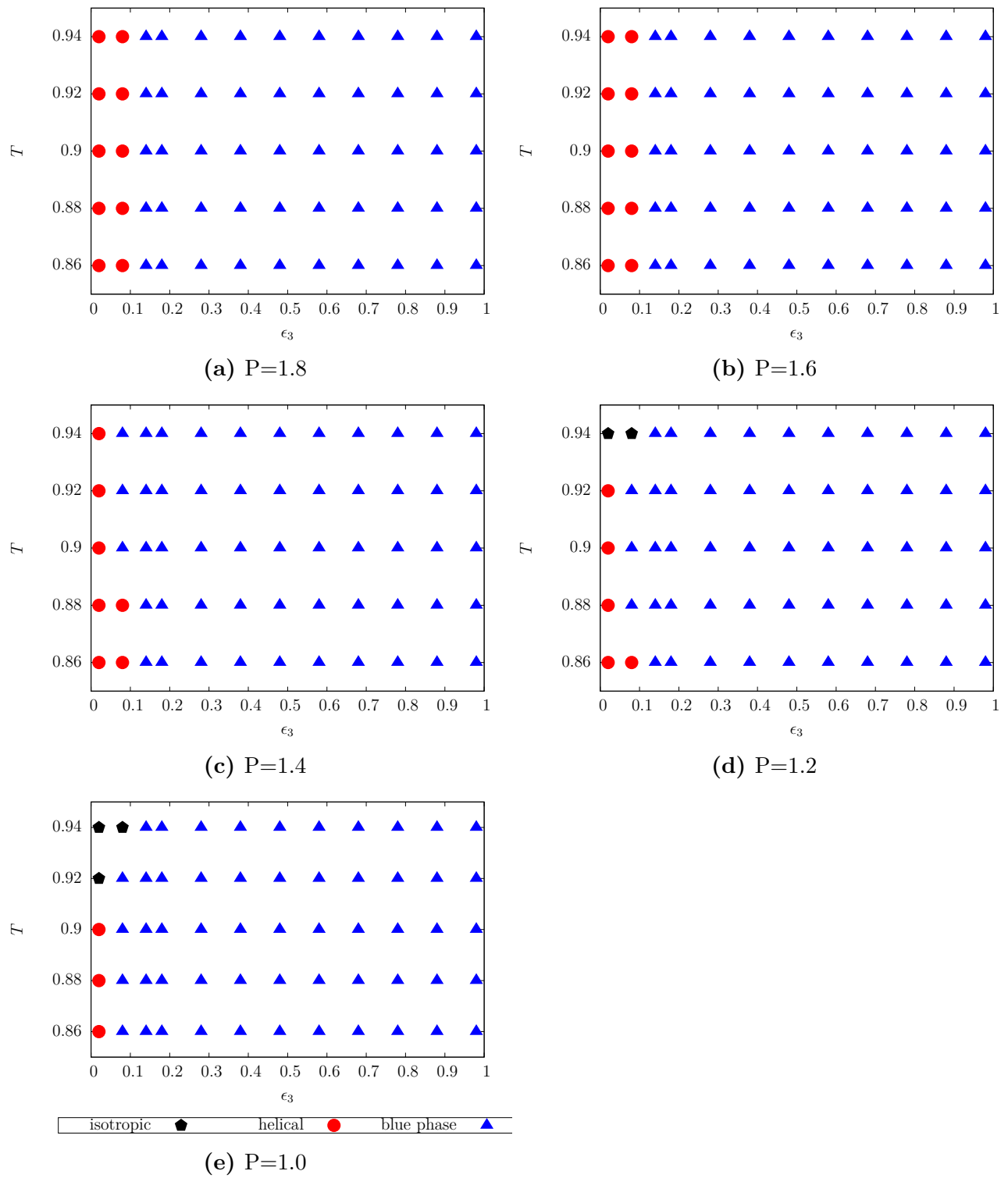
(c) P=1.4

(d) P=1.2

(e) P=1.0

Figure 4.21: Temperature-chirality phase diagrams for different pressures. The stability of blue phases increases with the chirality.

4.5 Flow profile

In order to characterize and describe the dynamic state of our system, we will use the dynamic viscosity η. Within the weak-flow limit for a planar Poiseuille flow of a uniform fluid with constant average density $\bar{\rho}$, one can calculate the steady state streaming velocity as presented in Equation (2.15). Now we can calculate η by fitting the velocity profile with a second-order even polynomial $v_x(z) = c_2 z^2 + c_0$, in analogy to Stieger et al. [30]. Hence, the resulting viscosity is $\eta = -\bar{\rho} F_{flow}/2c_2$. This procedure is done for the simulation time $t = 500\,000$, to get as close to a steady state as possible. The results for the viscosity η and the Reynolds number $\mathcal{R}$ for different external driving forces are presented in Table 4.2. The flow profiles for the times $t = 100\,000, 200\,000, 300\,000, 400\,000,$ and $500\,000$ are presented in Figures 4.22 - 4.24. Furthermore, the viscosity of the system decreases with increased stream velocity, as expected for a non-Newtonian liquid and the overall small Reynolds number indicates a laminar flow. The second-order polynomial provides a good fit for the center of the system channel but deviates from the data for the external forces $F_{flow} = 0.2$ and $F_{flow} = 0.4$ closer to the walls (see Fig. 4.23 and Fig. 4.24). For all tested flows a steady-state is reached after $t = 200\,000$.

F_{flow}	v_∞	η	$\mathcal{R}$
0.1	0.09	166.97	0.019
0.2	0.21	150.07	0.049
0.4	0.57	129.54	0.153

Table 4.2: Reynolds number $\mathcal{R}$ and viscosity η for different external driving forces F_{flow} and the corresponding steady state streaming velocities v_∞ used for the system $\epsilon_3 = 0.78$, $T = 0.94$, $P = 1.8$.

(a) $t = 100000$

(b) $t = 200000$

(c) $t = 300000$

(d) $t = 400000$

(e) $t = 500000$

Figure 4.22: Flow profile for $F_{flow} = 0.1$ for $\epsilon_3 = 0.78$, $T = 0.94$ and $P = 1.8$. Data points in black circles and corresponding least-square fit as red line.

(a) $t = 100000$

(b) $t = 200000$

(c) $t = 300000$

(d) $t = 400000$

(e) $t = 500000$

Figure 4.23: Flow profile for $F_{flow} = 0.2$ for $\epsilon_3 = 0.78$, $T = 0.94$ and $P = 1.8$. Data points in black circles and corresponding least-square fit as red line.

(a) $t = 100000$

(b) $t = 200000$

(c) $t = 300000$

(d) $t = 400000$
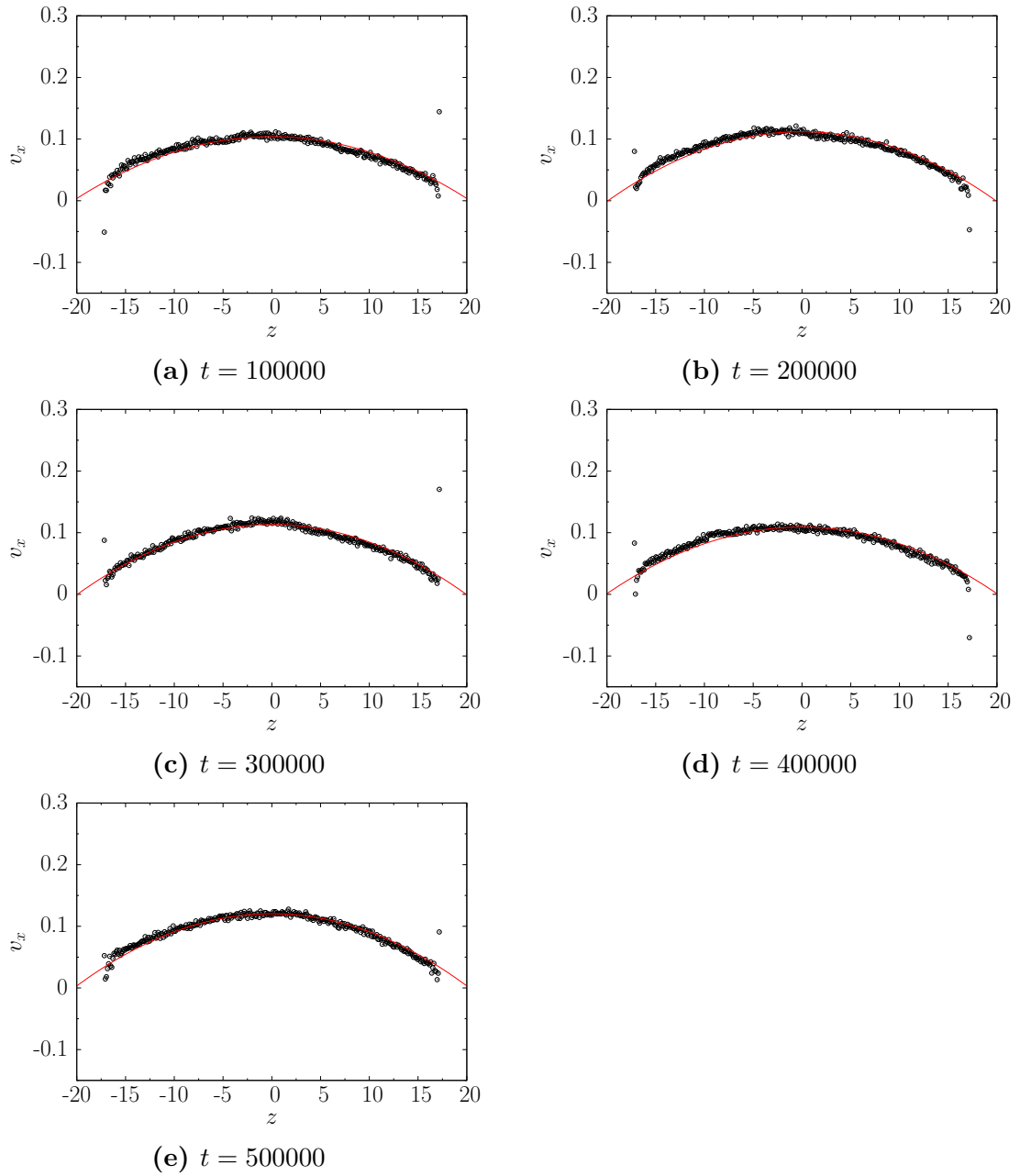
(e) $t = 500000$

Figure 4.24: Flow profile for $F_{flow} = 0.4$ for $\epsilon_3 = 0.78$, $T = 0.94$ and $P = 1.8$. Data points in black circles and corresponding least-square fit as red line.
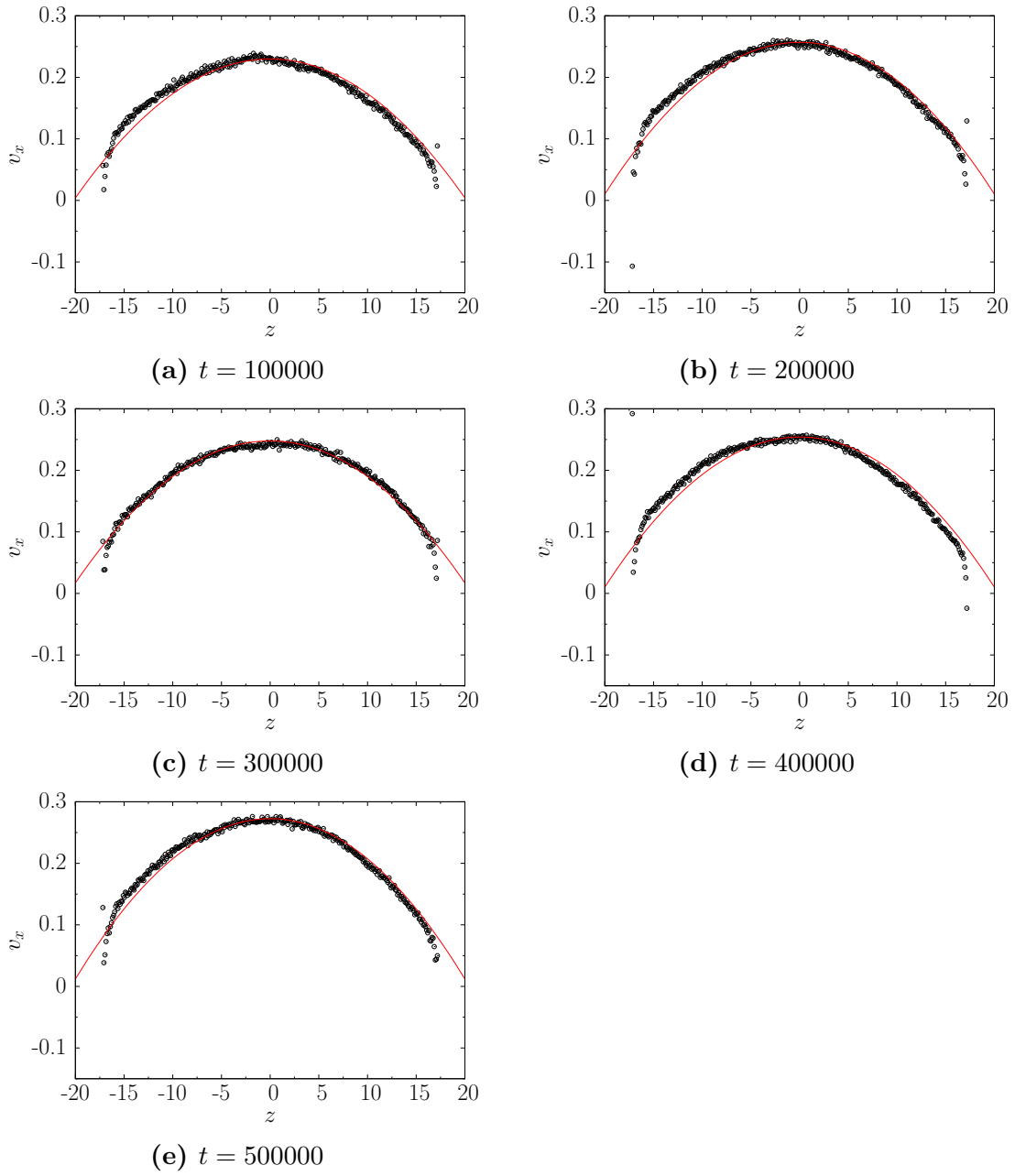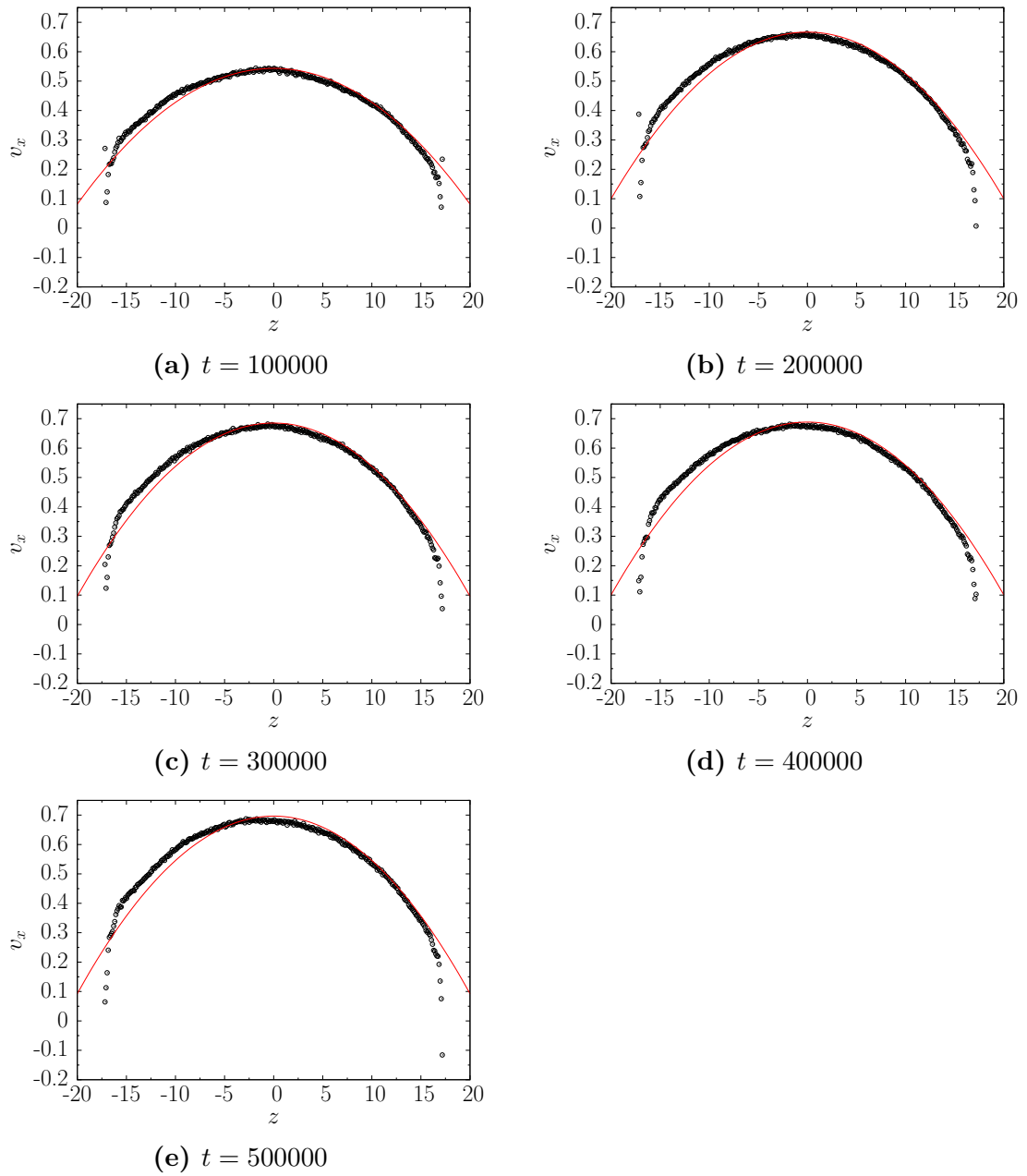
5 Discussion

5.1 NPT pitch

The measurement of the pitch and the classification in blue phase or helical phase in the NPT ensemble is overall accurate and in agreement with the snapshots of the system. The error of the least-squares fit is always $\leq 1\,\%$. As seen in Fig. 4.2, the nematic order parameter is atypically high at the lower wall for blue phases. Yet it decreases along the z-axis of the simulation box. This is a result of the anchoring function Eq. (2.7). Since hybrid anchoring is employed, the mesogens located close to the lower substrate will align preferably with the x-axis of the system. This results in a higher nematic order parameter at the lower substrate. Furthermore, the inverse proportionality of the pitch in dependency of the chirality has been shown, with parameters that are in the same order of magnitude as presented by Schlotthauer et al. [23]. However, functional dependencies of the temperature and pressure could not be found. In order to do so, one should perform more simulations with a wider range of temperature and pressure, as Fig. 4.7(a) and Fig. 4.7(b) suggest.

5.2 Pressure deviation between NPT and NVT simulations

As already mentioned, the pressure in an NVT ensemble directly results from the Helmholtz free energy, as presented in Eq. (3.1). Since the parameters used in the NVT simulations are determined under equilibrium of pressure, temperature and particle number, we expect the pressure of the NVT simulations P_{NVT} to be similar to the pressure of the NPT simulations P_{NPT}. Yet the direct measurement of the average pressure in the NVT ensemble shows a higher deviation from the desired pressure than the deviation from the pressure in the NPT ensemble (see Tab. 5.1). The average percentage deviation from the desired pressure is $\bar{\Delta}_{NPT} = 1.7\,\%$ for the

ϵ_3	T	P_{NPT}	P_{NVT}	Δ_{NPT}	Δ_{NVT}
0.18	0.86	1.005(4)	0.932(4)	0.5 %	6.8 %
0.18	0.90	1.410(4)	1.349(4)	0.7 %	3.6 %
0.18	0.94	1.821(4)	1.690(3)	1.2 %	6.1 %
0.48	0.86	1.003(4)	0.889(4)	0.3 %	11.1 %
0.48	0.90	1.418(4)	1.296(4)	1.3 %	7.4 %
0.48	0.94	1.826(5)	1.688(4)	1.4 %	6.2 %
0.78	0.86	0.942(5)	0.875(6)	5.8 %	12.5 %
0.78	0.90	1.430(5)	1.603(6)	2.1 %	14.5 %
0.78	0.94	1.827(5)	2.001(6)	1.5 %	11.2 %

Table 5.1: Comparison between average pressure in NPT simulations to the average pressure of corresponding NVT simulations. The average was taken for the last 100 000 time steps for each ensemble. The error results from the standard deviation. The percentage deviation for the NPT and the NVT ensemble Δ_{NPT} and Δ_{NVT} are calculated from the corresponding pressures $P = 1.0$, $P = 1.4$ and $P = 1.8$.

NPT pressure and $\bar{\Delta}_{NVT} = 8.8\,\%$ for the pressure in the NVT ensemble. From that we can deduce that the accuracy of the barostat is $\leq 1.7\,\%$. Since the volume of the simulation box in NVT was chosen to have an integer number of pitch lengths in each dimension, and the pitch is prone to errors and then cubed, the higher deviation from the desired pressure in the NVT ensemble results most likely from an error in the estimation of the appropriate volume used for the NVT simulations.

5.3 NVT disclination lines

When looking at the disclination lines of the system, one has to keep the results presented in Tab. 5.1 mind. Since the structure of the system is highly sensitive to pressure, temperature and chirality, the shown disclination lines (see Ch. 4.2) are accurate in the context of the deviation of the pressure.

5.4 Radial orientation functions

The radial orientation functions, especially the radial distribution function, are crucial to verify that the system is still in the liquid state. Otherwise are statements about phase transitions invalid and lead to wrong conclusions. As we can see in Fig. 4.16 the given model has the tendency to freeze for large chirality and low temperature and pressure. One has to keep that in mind when looking at the phase

diagrams in that parameter region.

5.5 Phase diagram

The presented phase diagrams show that we have been able to successfully reproduce the expected phase transitions. Furthermore, we could verify the temperature dependency of the phases of chiral liquid crystals. In addition, we could show that also the change of pressure can reproduce the same phase transitions for small chiralities (see Fig. 4.20). Yet one has to treat the accuracy of the phase diagrams with caution. Since the classification was done by visual inspection and supported with the results of the previous analysis, a more detailed differentiation between the phases, especially between the three distinct phases BP I, BP II and BP III, was not possible. In order to do this, various radial orientational pair correlation functions have to be analyzed for all parameter setups. This would go far beyond the scope of this thesis.

5.6 Flow profile

The Reynolds numbers (see Tab. 4.2) for the given system are in the same order of magnitude as presented from Stieger et al. [30] for a nematic system and indicate a laminar flow. Yet the dynamic viscosity is up to three times higher for similar steady-state streaming velocities v_∞. This is in total agreement with the fact that the blue phase can exhibit a up to 10^6 higher viscosity in comparison to a conventional fluid [10].

6 Summary

In this work, we employ molecular dynamics simulations in the canonical and isothermal- isobaric ensemble to investigate the properties of blue phases, a highly complex distinct phase of chiral liquid crystals. We show that the chiral version of the Hess-Su potential is capable of reproducing helical and blue phases for a various range of temperature, pressure and chirality values and present the results in detailed phase diagrams. The phase diagrams show phase transitions from the helical phase into the blue phase into the isotropic phase when increasing the temperature. In addition the same phase transitions can be observed for low chirality when decreasing the pressure.

Furthermore, the phase diagrams indicate that higher values of chirality have a stabilizing effect on the blue phase and make it less sensitive to temperature and pressure changes. The investigation of the pitch shows that the pitch is overall inversely proportional to the chirality ϵ_3 for all combinations of pressure and temperature used in this thesis. Yet a clear functional dependency between pressure and pitch or temperature and pitch has not been found and seems rather complex.

The disclination lines show that the structure of the studied blue phases is characterized by a three-dimensional simple-cubic lattice which is indicative for a blue phase II. This is supported by the radial distribution functions. They clearly show that the given system is locally highly ordered but globally isotropic, as expected from a blue phase. For a chirality $\epsilon_3 = 0.18$ the disclination lines show a tangled, rather spaghetti-like structure. This indicates a blue phase III. Yet the radial distribution functions do not indicate a distinct BP III.

The addition of a constant hydrodynamic flow show that the system is in a laminar regime for the investigated driving forces and exhibit a high viscosity, as expected for blue phases driven out of equilibrium.

Bibliography

[1] P.-G. de Gennes and J. Prost, *The Physics of Liquid Crystals* (Clarendon Press, 1993).

[2] C. Kittle, *Introduction to Solid State Physics* (John Wiley & Sons, 1995).

[3] PubChem, "Open chemistry database - ppa," (2015).

[4] PubChem, "Open chemistry database - mbba," (2015).

[5] D. C. Wright and N. D. Mermin, Reviews of Modern Physics **61** (1989).

[6] Heimopnnath, "Cholesteric scheme," (2005).

[7] P. P. Crooker, in *Chirality in Liquid Crystals*, Partially Ordered Systems (Springer New York, 2001) pp. 186–222.

[8] D. Armitage and F. Price, Journal de Physique Colloques **36**, 133 (1975).

[9] J. Thoen, Physical Review A **37**, 1754 (1988).

[10] H. Stegemeyer and P. Pollmann, Molecular Crystals and Liquid Crystals **82**, 123 (1982).

[11] P. E. Cladis, P. Pieranski, and M. Joanicot, Physical Review Letters **52**, 542 (1984).

[12] N. A. Clark, S. T. Vohra, and M. Handschy, Physical Review Letters **52**, 57 (1984).

[13] R. M. Hornreich and S. Shtrikman, Physical Review Letters. **56**, 1723 (1986).

[14] R. M. Hornreich, M. Kugler, and S. Shtrikman, Physical Review Letters **48**, 1404 (1982).

[15] P. J. Collings, Physical Review A **30**, 1990 (1984).

Bibliography

[16] D. Frenkel and B. Smit, eds., *Understanding Molecular Simulation (Second Edition)*, 2nd ed. (Academic Press, San Diego, 2002).

[17] S. Hess and B. Su, Zeitschrift für Naturforschung A. **54**, 559 (1999).

[18] R. Memmer, H.-G. Kuball, and A. Schönhofer, Liquid Crystals **15**, 345 (1993).

[19] R. Memmer, H.-G. Kuball, and A. Schönhofer, Molecular Physics **89**, 1633 (1996).

[20] M. Melle, M. Theile, C. Hall, and M. Schoen, International Journal of Molecular Sciences **14**, 17584 (2013).

[21] M. Melle, S. Schlotthauer, M. G. Mazza, S. H. L. Klapp, and M. Schoen, The Journal of Chemical Physics **136**, 194703 (2012).

[22] H. Steuer, S. Hess, and M. Schoen, Physical Review E **69**, 031708 (2004).

[23] S. Schlotthauer, R. A. Skutnik, T. Stieger, and M. Schoen, The Journal of Chemical Physics **142**, 194704 (2015).

[24] T. Gruhn and M. Schoen, Physical Review E **55**, 2861 (1997).

[25] R. Memmer, The Journal of Chemical Physics **114**, 8210 (2001).

[26] B. D. Todd, D. J. Evans, and P. J. Daivis, Physical Review E **52**, 1627 (1995).

[27] M. Greschek, M. Melle, and M. Schoen, Soft Matter **6**, 1898 (2010).

[28] S. D. Stoyanov and R. D. Groot, Journal of Chemical Physics **122**, 114112 (2005).

[29] M. Ravnik, P. A. Gareth, J. M. Yeomans, and S. Žumer, Proceedings of the National Academy of Sciences of the United States of America **108**, 5188 (2011).

[30] T. Stieger, M. Schoen, and M. G. Mazza, The Journal of Chemical Phsics **140**, 054905 (2014).

Acknowledgments

Erklärung nach §13(8) der Prüfungsordnung für den Bachelor-Studiengang Physik und den Master-Studiengang Physik an der Universität Göttingen:

Hiermit erkläre ich, dass ich diese Abschlussarbeit selbständig verfasst habe, keine anderen als die angegebenen Quellen und Hilfsmittel benutzt habe und alle Stellen, die wörtlich oder sinngemäß aus veröffentlichten Schriften entnommen wurden, als solche kenntlich gemacht habe.

Darüberhinaus erkläre ich, dass diese Abschlussarbeit nicht, auch nicht auszugsweise, im Rahmen einer nichtbestandenen Prüfung an dieser oder einer anderen Hochschule eingereicht wurde.

Göttingen, den 19. Oktober 2015

(Vitali Telezki)